Selective hydrogen atom abstraction from dihydroflavonol is the key step in the flavonol synthesis enzyme and avoids by-products

Document Version
Accepted author manuscript

[Link to publication record in Manchester Research Explorer](#)

OPEN ACCESS

Selective hydrogen atom abstraction from dihydroflavonol is the key step in the flavonol synthesis enzyme and avoids by-products.

Sidra Ghafoor,[§,‡] Asim Mansha,[‡] and Sam P. de Visser*,[§]

[§] The Manchester Institute of Biotechnology and Department of Chemical Engineering and Analytical Science, The University of Manchester, 131 Princess Street, Manchester M1 7DN, United Kingdom

[‡] Department of Chemistry, Government College University Faisalabad, New Campus, Jhang Road, Faisalabad, Pakistan

ABSTRACT: The plant nonheme iron dioxygenase flavonol synthase performs a regioselective desaturation reaction as part of the biosynthesis of the signaling molecule flavonol that triggers the growing of leaves and flowers. These compounds also have health benefits for humans. Desaturation of aliphatic compounds generally proceeds through two consecutive hydrogen atom abstraction steps from two adjacent carbon atoms and in nature often is performed by a high-valent iron(IV)-oxo species. We show that the order of the hydrogen atom abstraction steps; however, are opposite of those expected from the C-H bond strengths in the substrate and determines the product distributions. As such flavonol synthase follows a negative catalysis mechanism. Using density functional theory methods on large active site model complexes we investigated pathways for desaturation and hydroxylation by an iron(IV)-oxo active site model. Against thermochemical predictions, we find that the oxidant abstracts the hydrogen atom from the strong C^2–H bond rather than the weaker C^3–H bond of the substrate first. We analyzed the origin of this unexpected selective hydrogen atom abstraction pathway and find that the alternative C^3–H hydrogen atom abstraction would be followed by a low-energy and competitive substrate hydroxylation mechanism hence, should give considerable amount of by-products. Our computational modelling studies shows that substrate positioning in flavonol synthase is essential as it guides the reactivity to a chemo- and regioselective substrate desaturation from the C^2–H group leading to desaturation products efficiently.

INTRODUCTION.

Metalloenzymes have key functions to all living organisms, including plants, animals and bacteria; and catalyze vital reactions as defense mechanisms, but are also involved in biosynthesis and metabolism processes. There are many varieties of metalloenzymes in nature with varying numbers of metal ions and the number of those in the active site. Due to its large natural abundance a large number of metalloenzymes contain an iron center and of the mononuclear iron enzymes two classes exist, namely the heme and nonheme iron enzymes. The heme-iron enzymes range from peroxidases, catalases to monoxygenases and are highly diverse.[1-10] They all contain an iron embedded in a tetradentate ligated heme group, which leaves two binding sites (axial and distal to the iron) available in octahedral symmetry, whereby the axial ligand binds the heme to the protein and the distal site dioxygen. By contrast, nonheme iron dioxygenases have a more varied iron coordination environment that is either octahedral or trigonal bipyramidal and often bind the metal through a facial 2-His/1-Asp protein linkage.[11-13] The mononuclear nonheme iron enzymes have a broad range of functions in Biosystems that covers aerobic respiration, oxygen sensing, electron and small molecule transport as well as catalysis.[14-18] Generally, the nonheme iron dioxygenases utilize molecular oxygen on an iron center and their roles include the biosynthesis of natural products to the biodegradation of toxic compounds.[19-25] They typically react by oxygen atom transfer to substrates through aliphatic hydroxylation, aromatic hydroxylation as well as epoxidation.

A large subclass of the nonheme iron enzymes are the α-ketoglutarate dependent dioxygenases, which utilize dioxygen and α-ketoglutarate on a nonheme iron active site.[26-29] In their catalytic cycle dioxygen reacts with α-ketoglutarate to form succinate, CO_2 and a high-valent iron(IV)-oxo species. For taurine/α-ketoglutarate dependent dioxygenase (TauD) this iron(IV)-oxo species was one of the first that was trapped and characterized with UV-Vis absorption, EPR and Mössbauer spectroscopic tech-

1

niques.[30,31] Moreover, kinetic studies of these iron(IV)–oxo species found them to react with substrate efficiently through, e.g., substrate hydroxylation with a rate-determining hydrogen atom abstraction step.[13-16,32]

In plants, nonheme iron dioxygenases have important functions related to signaling processes that trigger the growth of leaves and flowers, although some deal with stress responses.[33-36] In particular, flavonoids are synthesized by a cascade of enzymes that includes several non-heme iron dioxygenases.[26,33-41] Thus, flavanone-3β-hydroxylase (FHT) takes flavanone as a substrate and regio- and stereoselectively hydroxylates the C^3-position of the substrate to form dihydroflavonol (Scheme 1). Recently, we reported DFT calculations on a flavonone-3β-hydroxylase model and showed the selectivity to be determined by substrate positioning in the active site that enables a stereo- and chemoselective reaction process that prevents side reactions.[42]

flavanone
naringenin: R = H

dihydroflavonol
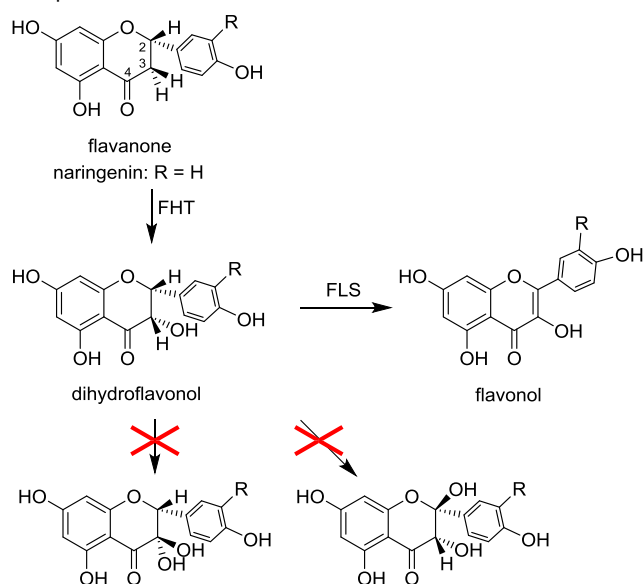
flavonol

Scheme 1. Conversion of flavanone into flavonol by FHT and FLS enzymes in plants.

In the next stage of the flavonol biosynthesis an unusual reaction takes place, whereby the dihydroflavonol is activated by flavonol synthase (FLS) and dehydrogenated (desaturated) at the C^2–C^3 bond to form flavonol products. Based on a combination of spectroscopic and crystal structure studies a mechanism was proposed, whereby the desaturation is performed by a high-valent iron(IV)–oxo species that sequentially abstracts two hydrogen atoms of the substrate:[43,44] one from the C^2 center and the other from the C^3 center. However, it is not clear in what order these hydrogen atoms are abstracted and whether the product distributions are different. Moreover, typical mechanisms catalyzed by iron(IV)–oxo species that start with a hydrogen atom abstraction are substrate hydrox-

ylation.[45,46] As far as we know, there exist no evidence of substrate hydroxylation side-products in wildtype FLS enzymes, i.e. the formation of C^2,C^3-dialcohol or C^3,C^3-dialcohol products have not been observed. To understand why hydroxylation reactions are prevented in favor of desaturation of dihydroflavonol, we decided to explore the reaction mechanism of dihydroflavonol activation by FLS leading to a variety of products as a result of desaturation and hydroxylation through attack on the C^2 as well as C^3 positions of substrate.

In previous work on heme monoxygenases, i.e. the cytochromes P450, we explored competitive substrate hydroxylation versus desaturation of drug molecules.[47] It was shown that, in general, substrate hydroxylation is favored due to the larger exothermicity of the hydroxylation reaction. As such, we would expect substrate hydroxylation to be the dominant channel in flavonol synthase enzymes rather than desaturation. How and why FLS can perform a thermochemically unfavorable desaturation reaction is currently unknown and warrants a detailed computational study. To gain insight into the regioselective biosynthesis reaction of FLS, we performed a computational study on a large active site model of FLS. It is shown that substrate positioning is essential and guides the reaction to the strong C^2–H bond. This is important as it will lead to preferential desaturation with a large conjugated π-system.

Methods.

Our work continues from our previous study on flavanone-3β-hydroxylase.[42] We took the crystal structure coordinates of FLS from the protein data bank, i.e. 2BRT pdb file,[44,48] and followed set-up procedures as described in detail previously.[49-51] The pdb structure contains the full protein (one monomer), with iron(II), α-ketoglutarate and naringenin bound. Iron(II)-water was replaced by iron(IV)-oxo and α-ketoglutarate with succinate to create the proposed high-valent oxidant in the reaction mechanism. We then removed naringenin from the pdb file and replaced it with dihydroflavonol, which was docked into the substrate binding pocket with Swissdock.[52] An overlay of the five conformations with the largest binding energy is shown in Figure S1 (Supporting Information) and as follows in all of those the substrate is in roughly the same position with the phenol group parallel to the aromatic ring of Phe_{144}. We chose a substrate binding orientation with the C^2–H and C^3–H groups of the substrate positioned in the vicinity of the iron(IV)-oxo group. Subsequently, hydrogen atoms were added to the pdb structure in Chimera based on a pH = 7 environment and followed by equilibration.[53]
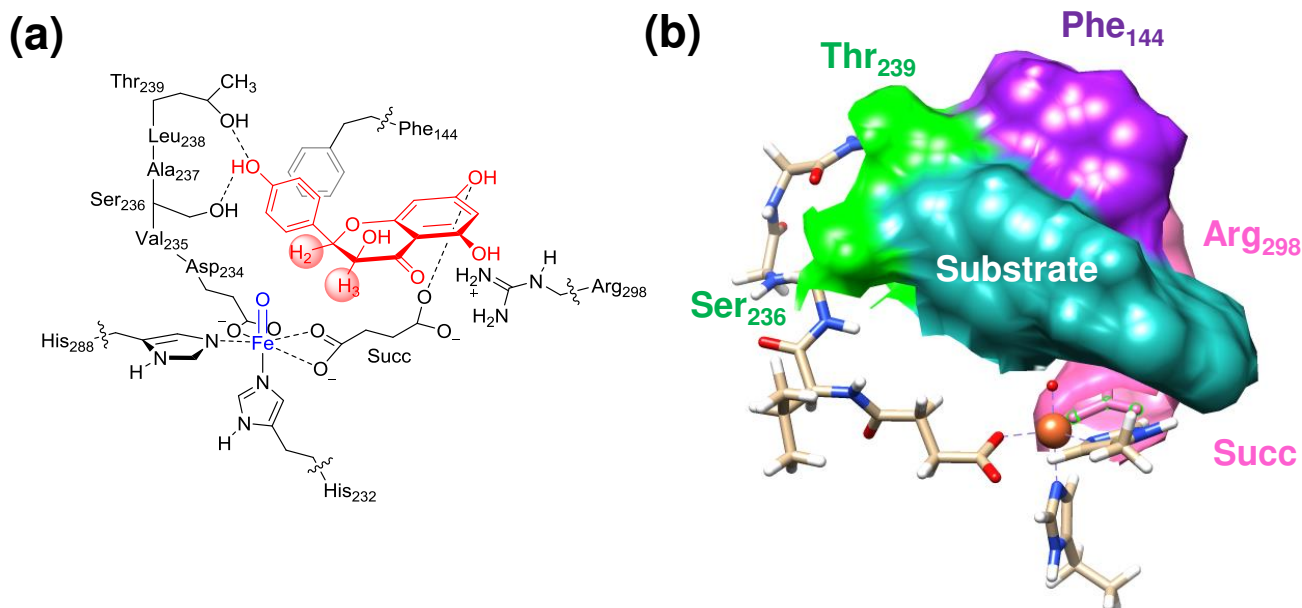
2

Figure 1. (a) Active site model of FLS as studied in this work. (b) Space filling model of substrate bound into the binding pocket of FLS.

Thereafter, a large cluster model was selected that included the iron with its first-coordination sphere of ligands, the substrates and key amino acid residues of the protein, including the chain Asp$_{234}$-Val$_{235}$-Ser$_{236}$-Ala$_{237}$-Leu$_{238}$-Thr$_{239}$, whereby the Ala and Leu residues were abbreviated to Gly in the model (see Figure 1a). The model contains iron(IV)-oxo, methylimidazole for His$_{288}$, ethylimidazole for His$_{233}$, a methylguanidine for Arg$_{298}$ and ethylbenzene for residue Phe$_{144}$. Our calculated FLS model had 170 atoms and was studied in the odd spin state, namely triplet and quintet, and has neutral charge. No geometry constraints were put on the model as substrate and protein are tightly bound in the pocket through a number of hydrogen bonding interactions (Figure 1b). Also an overlay of starting and optimized structures showed little geometric movements of the protein residues in the optimized geometries and hence little changes with respect to the crystal structure starting point were found.

Computational studies were performed using the Gaussian-09 program package with density functional theory.[54] Geometry optimization, geometry scans and analytical frequencies were done using the unrestricted hybrid density functional method UB3LYP.[55,56] A double-ζ quality basis set with 6-31G on all the atoms except Fe, which was described with an LACVP basis set with core potential (basis set BS1).[57-59] Local minima were characterized with a frequency calculation that gave real frequencies only, while transition states had one imaginary frequency for the correct mode. For key transition states also intrinsic reaction coordinate scans were performed that led in one direction

to products, while in the reverse direction optimized into the reactant complexes. The final structure of the IRCs was fully optimized (without constraints) for the radical intermediates ($^5IM_{2,\sigma}$ and $^5IM_{3,\sigma}$) and a geometry with energy was obtained that was close to the one reported below, see Supporting Information. Single point energy calculations were done using the LACV3P+ basis set on iron (with core potential) and 6-311+G* on the remaining atoms (basis set BS2) to improve the energetics of the chemical system. Solvent effects were included using the continuum polarized conductor model with a dielectric constant mimicking chlorobenzene.[60] Free energies reported here contain zero-point, solvent, entropic and thermal corrections (to 298K) as taken from the Gaussian frequency files. The methods used in this work were tested and validated previously and reproduced experimental rate constants, chemoselectivities and spectroscopic parameters well.[61-63] In one of those studies,[61] experimentally obtained free energies of activation for substrate activation by iron(IV)-oxo complexes were compared to computation. These studies showed improved performance of B3LYP over B3LYP-D3 for these types of systems. Nevertheless, we optimized several structures with B3LYP-D3[55,56,64] (Supporting Information) and although the barriers are somewhat lower than those at B3LYP level of theory, the trends were the same. All transition states reported here had a single imaginary frequency for the correct mode, while local minima had real frequencies only.

Kinetic isotope effects (KIE) were calculated from the Gaussian frequency files, whereby the vibrational fre-

3

quencies, entropy and free energy of activation were re-calculated with protiums replaced by deuterium. KIEs were calculated from the classical Eyring equation (KIE$_E$, Eq. 1), while tunneling corrections to the KIE were obtained through the Wigner correction (KIE$_W$, Eqs. 2 and 3).[65] The KIE$_E$ is determined by the difference in the Gibbs free energy ($\Delta G^\ddagger$) of the protium and deuterium-substituted system, where R represents the gas constant and T the temperature of the system (298K). Although quantum tunneling effects can be very large for deuterium substituted reactions, previous work showed the Wigner model to predict KIEs in reasonable agreement with experiment.[66,67]

To obtain the Wigner KIE$_W$ we took the Eyring KIE$_E$ and multiplied it with the tunneling correction Q$_t$, which is determined from the imaginary frequency in the transition state (v in cm^{-1}), Planck's constant (h), the Boltzmann constant (k$_B$) and the temperature of the system.

$$KIE_E = \exp\left[(\Delta G^\ddagger_D - \Delta G^\ddagger_H)/RT\right] \qquad (1)$$

$$KIE_W = KIE_E \times Q_{t,H}/Q_{t,D} \qquad (2)$$

$$Q_t = 1 + (hv/k_BT)^2/24 \qquad (3)$$

RESULTS.

Based on the crystal structure coordinates of FLS,[44] a cluster model was created as described in Figure 1. A space-filling model of the substrate-bound reactant structure is shown in Figure 1b, which highlights key interactions of the substrate with protein. As can be seen, the substrate is tightly packed with π-stacking interactions to a neighboring aromatic ring of Phe$_{144}$, while it undergoes hydrogen bonding interactions with the alcohol groups of the side chains of Ser$_{236}$ and Thr$_{239}$ with its phenol group, whereas the two phenol groups of the resorcinol ring are in hydrogen bonding distance to the salt bridge between succinate and Arg$_{298}$. Overall, the substrate appears in a very rigid configuration so that little mobility and flexibility is expected. Nevertheless, the C^2–C^3 bond of the substrate in this orientation is pointing directly to the iron(IV)-oxo group.

We initially optimized the iron(IV)-oxo species (^{3,5}Re) in the low-lying triplet and quintet spin states and subsequently investigated hydrogen atom abstraction from either the C^2–H or C^3–H positions of substrate as identified with a pink circle in Figure 1a. These hydrogen atom abstraction barriers are labelled TS1$_{HA,2}$ and TS1$_{HA,3}$, respectively, and lead to the iron(III)-hydroxo intermediates IM$_2$ and IM$_3$ with a radical on carbon atom C^2 or C^3, respectively. Thereafter, a second hydrogen atom abstraction via transition state TS2$_{HA}$ can take place to form desaturated products (P$_D$) or alternatively OH rebound via transition state TS$_{reb}$ gives alcohol product complexes (P$_A$).

Before discussing the reaction mechanisms leading to these product complexes, let us first focus on the electronic configuration and geometry of the reactant complex. Optimized geometries of the triplet and quintet spin reactant complexes (^{3,5}Re) are shown in Figure 2. Similarly to previous computational studies on analogous iron(IV)-oxo complexes of nonheme iron enzymes[68-84] and experimental EPR and Mössbauer measurements of related nonheme iron dioxygenases,[30,31,85-87] the quintet spin state is the ground state. The ^{5}Re complex has an electronic configuration of $\pi^*_{xy}{}^1 \pi^*_{xz}{}^1 \pi^*_{yz}{}^1 \sigma^*_{x2-y2}{}^1$ with orbitals as shown in Figure 2b. These orbitals represent the metal-ligand interactions and particularly between the iron and oxo group. The σ^*_{z2} orbital is antibonding along the O–Fe–N(His$_{232}$) axis and virtual in the reactant state; thus giving the metal a formal oxidation state of iron(IV).

Because of this molecular orbital occupation, the Fe–O distance is short in ^{5}Re, i.e. 1.657Å. This value matches experimentally determined Fe^{IV}–O bond distances measured for taurine/α-ketoglutarate dioxygenase (1.62Å)[86] and α-ketoglutarate dependent halogenase CytC3 (1.60 – 1.62Å).[88] In ^{3}Re, on the other hand, the orbital occupation is $\pi^*_{xy}{}^2 \pi^*_{xz}{}^1 \pi^*_{yz}{}^1$, while both σ^* orbitals are virtual. As can be seen from the orbital drawing in Figure 2b, the π^*_{xy} orbital has some interactions with the 2p$_x$ and 2p$_y$ orbitals on the oxygen atom and hence occupation of this orbital with a second electron will put more antibonding character on the Fe–O interaction resulting in its elongation. Indeed a much longer Fe–O distance of 1.784Å is observed in the triplet spin state. The triplet spin state is considerably less stable in energy than the quintet by ΔG = 15.9 kcal mol^{-1} in the gas-phase and, hence, will not play a role of importance. This result matches previous work on the iron(IV)-oxo species of nonheme iron dioxygenases where the metal is in a trigonal bipyramidal arrangement with well separated quintet and triplet spin state structures.[64-70, 89-93] By contrast, with iron in octahedral coordination environment typically a triplet spin ground state is found with the quintet spin well higher in energy.[94-97]

The optimized geometry of the reactant structures also highlights key interactions of the substrate with the protein that lock it into position. Thus, the phenol group of the substrate forms hydrogen bonding interactions with the alcohol groups of Ser$_{236}$ and Thr$_{239}$. These distances (R1 and R2) are very short, namely 1.62 and 1.76Å, respectively, and, therefore, the bonding is strong. In addition, the aromatic ring of Phe$_{144}$ is positioned parallel to the aromatic ring of the substrate phenol group and hence will stabilize the position of the substrate through π-stacking interactions.
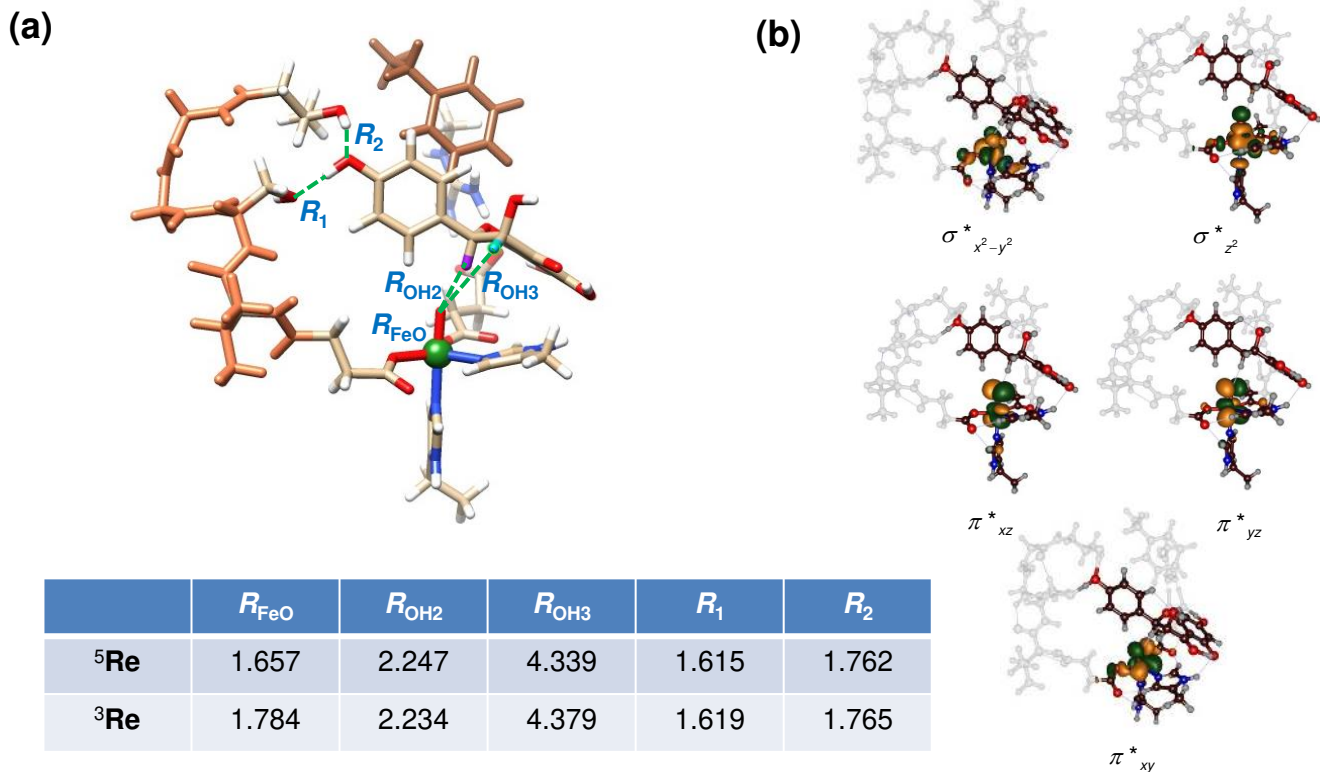
4

Figure 2. Optimized geometries and electronic configuration of the iron(IV)-oxo reactant complex of FLS as calculated at UB3LYP/BS1 in Gaussian-09. (a) Optimized ^{3,5}Re structures with bond lengths in angstroms. (b) Metal 3d-type orbitals of ^{5}Re.

	R_{FeO}	R_{OH2}	R_{OH3}	R_1	R_2
^{5}**Re**	1.657	2.247	4.339	1.615	1.762
^{3}**Re**	1.784	2.234	4.379	1.619	1.765

The resorcinol hydroxyl groups of the substrate are also involved in hydrogen bonding interactions and are closely located to the salt bridge between succinate and Arg$_{298}$ causing further stabilization and lock the substrate in an overall tight configuration. Indeed little geometric changes in the substrate positioning are seen during the full reaction mechanism and the individual geometry optimizations. The substrate positioning also points the C^2-H and C^3-H hydrogen atoms towards the iron(IV)-oxo group and sets them up for a regioselective hydrogen atom abstraction from those two positions. Due to the rigidity of the substrate in the binding pocket no other positions of the substrate can be activated unless several strong hydrogen bonding interactions are broken.

Next, we studied the hydrogen atom abstraction pathways starting from ^{5}Re for abstraction of an atom from the C^2-H and C^3-H bonds of the substrate. Electronically; however, there are several possible mechanisms on each of the spin state surfaces leading to multistate reactivity patterns as schematically depicted in Scheme 2. Thus, the hydrogen atom abstraction leads to transfer of one electron into the metal 3d-set of orbitals. Due to the close-lying configurations of the reactant and intermediate, i.e. iron(III)-hydroxo, states, several possibilities exist for this electron transfer from quintet spin reactants, namely by formation of a sextet spin iron(III)-hydroxo coupled with a down-spin electron on the substrate or alternatively a quartet spin iron(III)-hydroxo coupled to an up-spin electron on the substrate (Scheme 2). The former is designated the $^5\sigma$-pathway and the latter the $^5\pi$-pathway.[96-102] In the $^5\sigma$-pathway an electron is transferred from the substrate into the virtual σ^*_{z2} orbital that gives a fully exchange-enhanced metal 3d-block with five unpaired electrons and leaves a down-spin electron on the substrate to give an electronic configuration: $\pi^*_{xy}{}^1 3d_{xz}{}^1 \pi^*_{yz}{}^1 \sigma^*_{x2-y2}{}^1 \sigma^*_{z2}{}^1 \pi_{Sub}{}^1$. Generally, the elongation of the Fe-O bond in this step splits the π_{xz}/π^*_{xz} couple back into atomic orbitals, hence the $3d_{xz}$ is now occupied with one electron. It has been proposed that this always gives the lowest energy mechanism for nonheme iron(IV)-oxo complexes.[103] However, as shown previously, substrate and oxidant positioning as well as environmental perturbations can reverse the ordering and stabilize the $^5\pi$-pathways instead.[104] In the $^5\pi$-pathway the incoming electron from the substrate moves into the lowest of the metal 3d orbitals, namely the π^*_{xy} that becomes doubly occupied and the electronic configuration of the radical intermediate ^{5}IM$_2$, is $\pi^*_{xy}{}^2 3d_{xz}{}^1 \pi^*_{yz}{}^1 \sigma^*_{x2-y2}{}^1 \pi_{Sub}{}^1$ with the substrate radical up-spin. We attempted to calculate both reaction pathways (transition states and intermediates) for each of the hydrogen atom abstraction reactions.

5
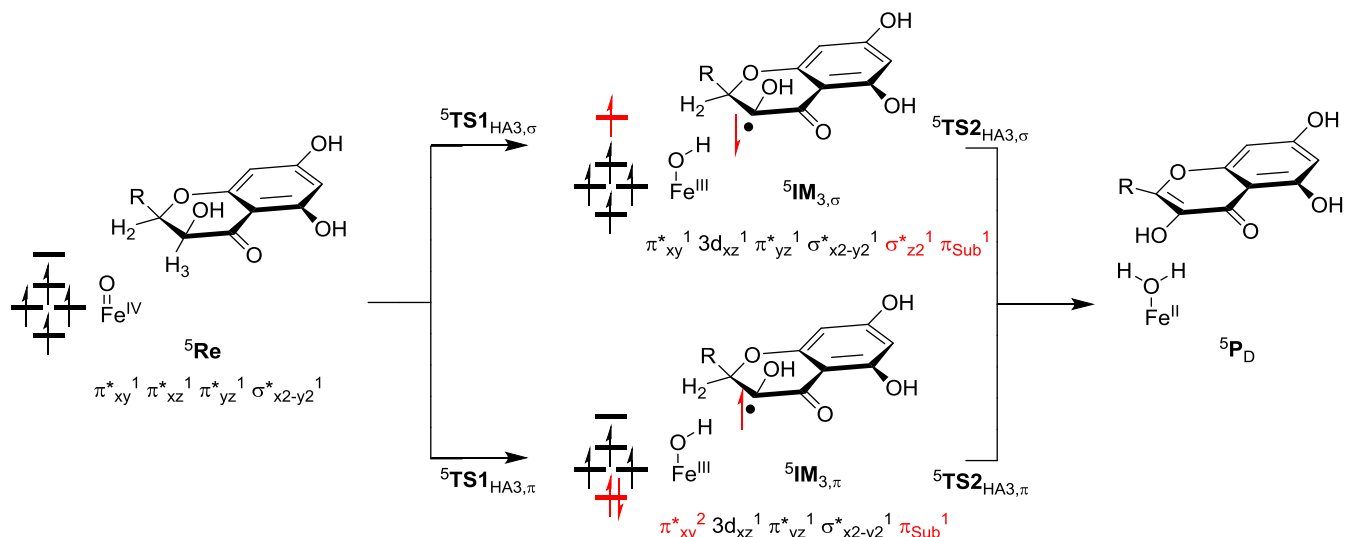
Scheme 2. Electron transfer pathways during the hydrogen atom abstraction steps leading to $^5\sigma$- and $^5\pi$ mechanisms.
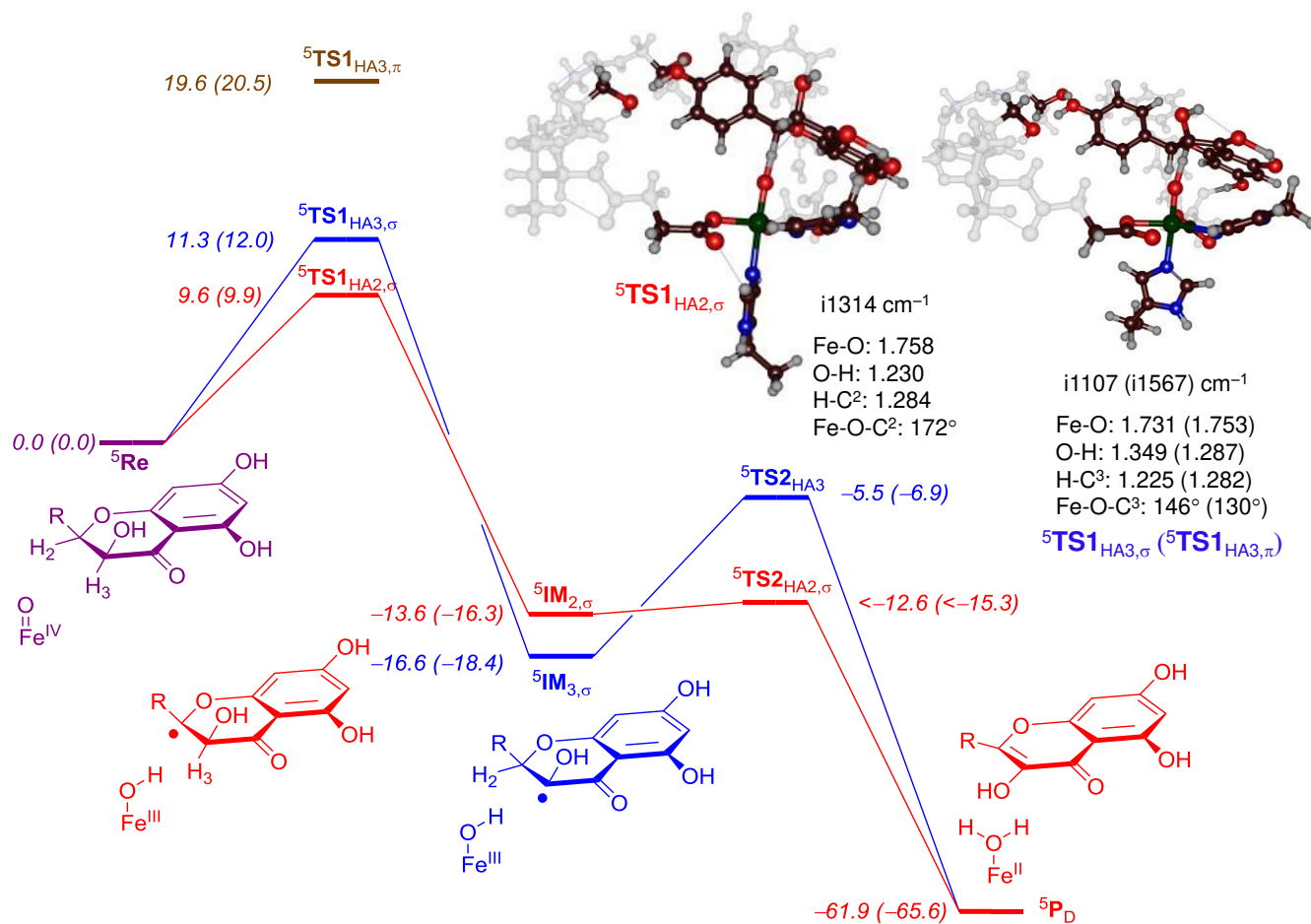
Figure 3. Potential energy landscape (with energies in kcal mol^{-1}) of dihydroflavonol desaturation to flavonol by the iron(IV)-oxo species of FLS. Energies are obtained at UB3LYP/BS1//UB3LYP/BS2 and contain ZPE and solvent corrections. Free energies are given in parenthesis and include thermal (at 298K), solvent and entropic corrections. Optimized geometries of rate-determining hydrogen atom abstraction transition states give bond lengths in angstroms and the imaginary frequency in cm^{-1}.

The calculated free energy landscape of dihydroflavonol desaturation by the iron(IV)-oxo species of FLS via the possible $^5\sigma$- and $^5\pi$-pathways are given in Figure 3. We investigated initial hydrogen atom abstraction from the C^2–H bond first and then followed by hydrogen atom abstraction from the C^3–H position, but the reverse order of hydrogen atom abstraction steps was also tested. These pathways are labeled with a subscript 2 or 3 in the structure for the first hydrogen atom abstraction site, respectively. Both $^5\sigma$ hydrogen atom abstraction barriers are lower in energy than the triplet spin reactants; hence the mechanism takes place on a dominant quintet spin state surface via single-state-reactivity. Indeed, the triplet spin pathways are high in energy and we find a barrier $^3TS1_{HA3,\sigma}$ of $\Delta G^\ddagger = 29.7$ kcal mol^{-1}, see Supporting Information. As such we will focus on the quintet spin pathways only.

The lowest energy transition state is for hydrogen atom abstraction from the C^2-position and has a free energy of activation of 9.9 kcal mol^{-1}. The substrate C–H bond is aligned to the Fe–O bond and the TS has an Fe–O–C^2 angle of 172°. As a $^5\sigma$-pathway involves transfer into the σ^*_{z2} orbital, a linear configuration has been proposed to be ideal for these types of pathways.[105,106] Consequently, the geometry of $^5TS1_{HA2,\sigma}$ is close to its ideal conformation for a $^5\sigma$-pathway. Geometrically, the transition state is central with almost equal C^2–H and O–H distances: 1.284 and 1.230Å, respectively. We tried to locate the $^5TS1_{HA2,\pi}$ transition state through swapping of molecular orbitals in $^5TS1_{HA2,\sigma}$; however, during the energy convergence it converted back to the σ-pathway transition state. Therefore, the $^5\pi$-pathway is a high-energy pathway and will not play a role of importance.

The alternative hydrogen atom abstraction pathways from the C^3–H position of substrate have barriers of $\Delta G^\ddagger = 12.0$ (20.5) kcal mol^{-1} via $^5TS1_{HA3,\sigma}$ ($^5TS1_{HA3,\pi}$). Accordingly, the $^5\pi$-pathway is high in energy and with a free energy difference of almost 10 kcal mol^{-1} this implies that the $^5\sigma$-pathway will be dominant. Indeed, a geometry optimization of the radical intermediate $^5IM_{2,\pi}$ failed to converge and relaxed to the lower energy $^5IM_{2,\sigma}$ structure instead. Geometrically, the Fe–O–C^3 angle is considerably bent: 146° for $^5TS1_{HA,\sigma}$ and 130° for $^5TS1_{HA,\pi}$. A small angle of around $120 - 130°$ is typically observed in π-type reaction channels as an electron transfer into a π^* orbital takes place and the orbital overlap with the donor is best in this orientation.[105,106] Interestingly, both transition states are relatively central with C^3–H and O–H distances that are close.

Hydrogen atom abstraction barriers generally encounter a large kinetic isotope effect (KIE) when the transferring hydrogen atom is replaced by deuterium. To find out what the KIE would be for the hydrogen atom abstraction path-

way via $^5TS1_{HA2,\sigma}$ and $^5TS1_{HA3,\sigma}$, we reevaluated the vibrational frequencies and entropies using a mass of deuterium for the transferring atom in ^5Re, $^5TS1_{HA2,\sigma}$ and $^5TS1_{HA3,\sigma}$. Using the Eyring and Wigner models at 298K we estimated the kinetic isotope effects. Values of 7.4 and 6.1 are found for the Eyring KIEs for $^5TS1_{HA2,\sigma}$ and $^5TS1_{HA3,\sigma}$, respectively, whereas the Wigner tunneling correction raises these values to 10.0 and 8.8. As such, our calculated KIE values implicate classical KIE contributions that are dominated by the Eyring correction to the free energy and some effect of tunneling enhances the KIE further as estimated from the Wigner KIEs. Moreover, there appears to be little difference in the KIE values for C^2–H or C^3–H hydrogen atom abstraction and consequently the KIE cannot distinguish the two pathways. Our calculated KIEs match previously calculated values of analogous processes well.[107]

After the transition states the structures relax to a radical intermediate $^5IM_2$ or $^5IM_3$; however, the energetic ordering of the intermediates is reversed with respect to those of the hydrogen atom abstraction transition states. The most stable one is $^5IM_{3,\sigma}$ and is $\Delta G = 18.4$ kcal mol^{-1} more stable than reactants. By contrast, the lowest hydrogen atom abstraction barrier TS1 connects to $^5IM_{2,\sigma}$, which is $\Delta G = 16.3$ kcal mol^{-1} more stable than the reactants complex. A geometry scan for the subsequent hydrogen atom abstraction from the C^3–H position of substrate by the iron(III)-hydroxo intermediate $^5IM_{2,\sigma}$ was performed (Supporting Information Figure S12) and gave a small barrier of less than 1 kcal mol^{-1} leading to dehydrogenated products. As such the first hydrogen atom abstraction via $^5TS1_{HA2,\sigma}$ is rate-determining and will lead to dehydrogenation efficiently with a very short lifetime of the radical intermediate. A similar mechanism for the hydrogen atom abstraction via the $^5\pi$-pathway from the C^2–H position of substrate was found, where the first hydrogen atom abstraction is rate-determining and followed by a small barrier of less than 1 kcal mol^{-1} for the second hydrogen atom abstraction.

Interestingly, the energy profile starting with hydrogen atom abstraction from the C^3–H position of substrate is very different and although the first step is rate-determining with a free energy of activation of 12.0 kcal mol^{-1}, actually, a significant second hydrogen atom abstraction barrier via $^5TS2_{HA3,\sigma}$ is found that is 11.5 kcal mol^{-1} above the energy of $^5IM_{3,\sigma}$. This will affect the observed kinetics of the reaction and; moreover, means the radical intermediate has a finite lifetime and could rearrange or give rise to side-reactions, for instance, leading to substrate hydroxylation instead. To find the competitive substrate hydroxylation pathway, we then calculated OH rebound to form the alcohol products.
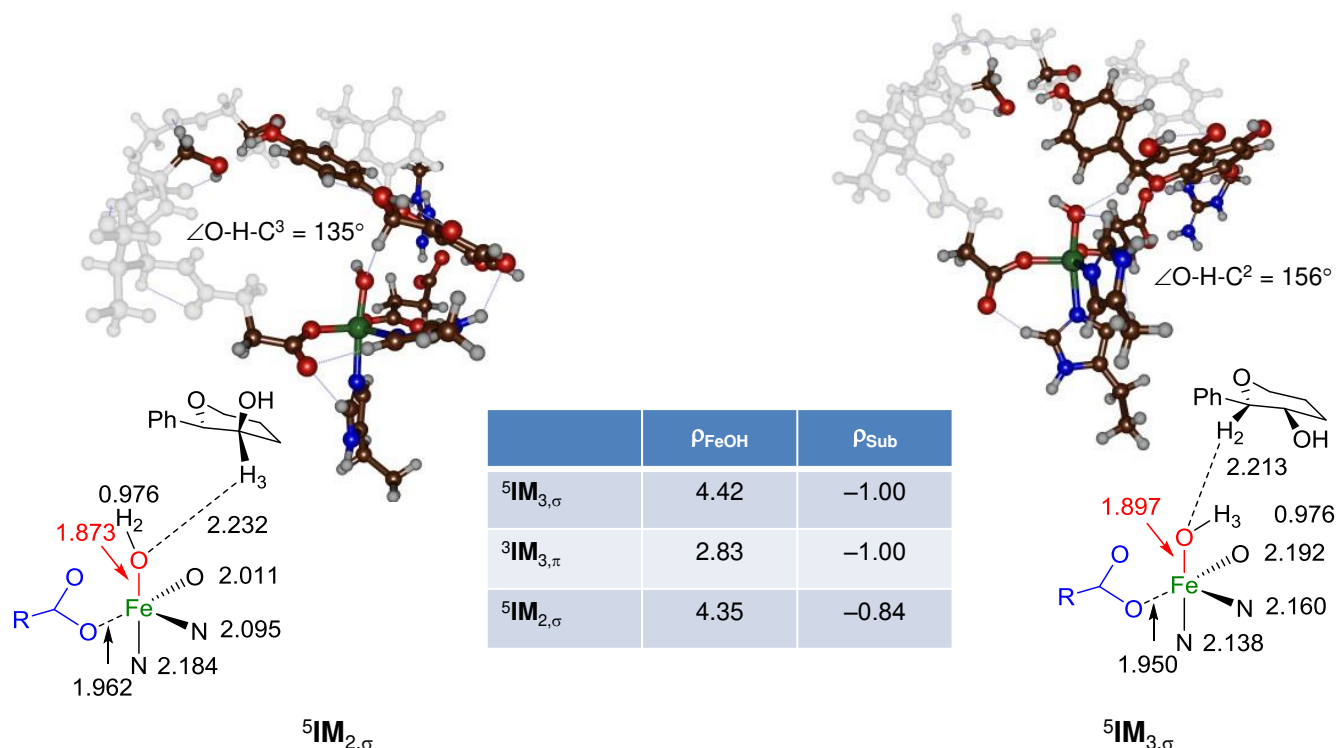
7

Figure 4. UB3LYP/BS1 optimized geometries of radical intermediates $^5IM_3$ and $^5IM_2$ as obtained in Gaussian-09. Bond lengths are in angstroms and group spin densities (ρ) in au.

	ρ_{FeOH}	ρ_{Sub}
$^5IM_{3,\sigma}$	4.42	−1.00
$^3IM_{3,\pi}$	2.83	−1.00
$^5IM_{2,\sigma}$	4.35	−0.84

The constraint geometry scan (see Supporting Information Figure S10) gives a maximum of around 12 kcal mol^{-1} for this pathway. Therefore, hydrogen atom abstraction from the C^3–H position leads to competitive hydroxylation and desaturation via similar reaction barriers.

To understand the differences in second hydrogen atom abstraction pathways between initial C^2–H and C^3–H hydrogen atom abstraction, we show in Figure 4 the optimized geometries of the radical intermediates $^5IM_{2,\sigma}$ and $^5IM_{3,\sigma}$. The Fe-O bond lengths are 1.873 and 1.897Å for $^5IM_{2,\sigma}$ and $^5IM_{3,\sigma}$, respectively, while the O-H distances are 0.976Å for both of them. Moreover, the first-coordination sphere ligand distances are relatively close. The spin on the FeOH group is 4.42 in $^5IM_{3,\sigma}$, while it is 4.35 in $^5IM_{2,\sigma}$. Therefore, the structures show no dramatic differences and hence provide no clear explanation why the second hydrogen atom abstraction barrier is so much larger in the C^2–H pathway. The only difference between the two pathways is that in $^5IM_{3,\sigma}$ a benzylic hydrogen atom is abstracted, whereas in $^5IM_{2,\sigma}$ a tertiary C–H bond is activated. To understand the order and nature of these hydrogen atom abstraction pathways, and why the second hydrogen atom abstraction barriers vary so strongly, we decided to calculate C–H bond strengths in the substrate of the neutral and radical complexes.

DISCUSSION.

In this work dihydroflavonol activation by the nonheme iron enzyme FLS is explored to give desaturation to form flavonol products. Our calculations predict an overall regiospecific dehydrogenation of substrate as the main reaction pathway in agreement with experimental observation.[44] The work shows an interesting reactivity pattern, where the kinetics favors C^2–H hydrogen atom abstraction over C^3–H hydrogen atom abstraction but the reverse is found for the thermodynamics of the reaction. Thus, the hydrogen atom abstraction barrier from the C^2–H position is favored over that of the C^3–H position, but the relative energies of the radical intermediates give a more stable C^3 radical than a C^2 radical (Figure 3). This is a unique example of the so-called negative catalysis, whereby a low-energy pathway is prevented in favor of another reaction.[108,109] Clearly, the enzyme was designed with the aim to react regiospecifically with substrates. Indeed, experimental reports on studies of substrate activation by FLS enzymes showed considerable substrate specificity.[38,110] In particular, mutations of the substrate binding pocket of FLS, e.g. where the Phe$_{144}$ was mutated, led to reduced activities and substrate conversion. Quite a number of studies have been reported that investigated substrate turnover using alternative (non-natural) substrates or substrate analogs.[111-115]
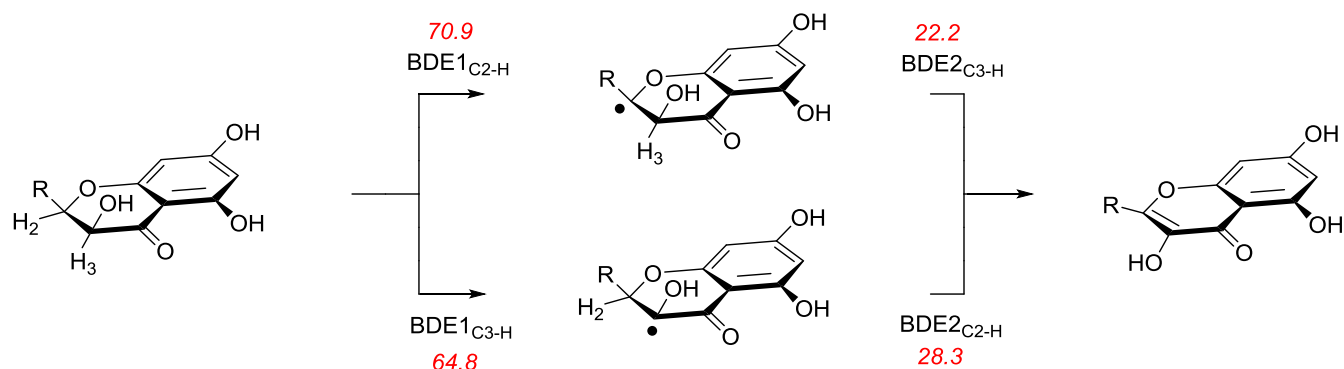
8

Figure 5. B3LYP/6-311++G** calculated C–H bond dissociation free energies (ΔG in kcal mol⁻¹) of dihydroflavonol substrate.

Thus, with alternative substrates often substrate hydroxylation rather than desaturation was observed. Moreover, Schofield et al[111] using these substrate analogs devised that substrate activation happens on the C^3-position. In agreement with these studies, our work shows that under ideal conditions, whereby substrate approach is not blocked through second-coordination sphere effects, its activation should take place on the C^3-position.

Our computational studies support the experimental work and show that the substrate is tightly bound in the pocket so as to enable the activation of the strongest of the two C–H bonds at C^3 and C^4. To understand the reaction mechanism and reaction rates and why these orderings change along the reaction mechanism, we decided to do a thermochemical and valence bond analysis of the transition state and intermediate structures along the reaction pathway. These thermochemical cycles and valence bond analysis were previously done to explain reactivity patterns by enzymatic and biomimetic oxidants and explained selectivities.[116,117]

We started with calculating the bond dissociation free energy (BDE) of various C–H bonds in the substrate (Sub–H) with the help of Eqs 4 and 5.
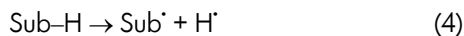
$$Sub–H \rightarrow Sub^\bullet + H^\bullet \qquad (4)$$
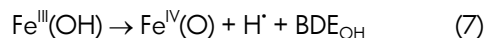$$-BDE_{CH} = \Delta G_{Eq\,4} = G_{Sub} + G_H - G_{Sub–H} \quad (5)$$

These BDEs were evaluated by calculating and optimizing the individual structures in the reaction mechanism according to Eq 4 at UB3LYP/6-311++G** level of theory. The free energies of these species were taken from the individual frequency calculations at 298K and the bond dissociation free energies were calculated for the C–H bond strengths of the C^2–H and C^3–H bonds in the substrate and hydrogen atom abstracted radicals. The obtained BDE values for the different C^2–H and C^3–H bond strengths are given in Figure 5, whereby the hydrogen atom abstraction from substrate is defined as BDE1 and the hydrogen atom abstraction from the radical is BDE2.

As can be seen from Figure 5 the free energy of activation of the C^2–H bond is 70.9 kcal mol⁻¹, while it is 64.8 kcal mol⁻¹ for the C^3–H bond. These two hydrogen atom abstraction steps are followed by another hydrogen atom abstraction leading to desaturation of the C–C bond to form flavonol products. Of course, the sum of the two hydrogen atom abstraction bond strengths, i.e. $BDE1_{C2}$ + $BDE2_{C3}$ versus $BDE1_{C3}$ + $BDE2_{C2}$, is the same as both reaction pathways start from the same reactant and give the same product, which means the energy difference between reactants and products must be equal. As follows, the energy to break a C–H bond in dihydroflavonol is costly, but abstracting a second hydrogen atom via BDE2 requires a very little amount of additional energy, namely $BDE2_{C3-H}$ = 22.2 kcal mol⁻¹, while $BDE2_{C2-H}$ = 28.3 kcal mol⁻¹. These low BDE2 values are the result of the formation of a strong π-bond between atoms C^2 and C^3, which is highly stabilized and in conjugation with a large π-system. The thermodynamic results from Figure 5 imply that in the gas-phase with an unperturbed system, a hydrogen atom abstraction from the weakest C–H bond, i.e. the C^3–H bond, would be expected as the dominant reaction pathway. Indeed, calculations of the reaction mechanism (Figure 3 above) indicate that the radical intermediate $^5IM_{3,\sigma}$ is lower in energy than $^5IM_{2,\sigma}$ in agreement with the relative stability of the substrate radicals. As such the DFT calculations on the enzymatic model follow the thermodynamics of the calculated bond strengths.

Based on the relative difference of the C^2–H and C^3–H BDE1 values; therefore, the weakest C–H bond should give the lowest hydrogen atom abstraction barrier as the overall reaction for hydrogen atom abstraction from an iron(IV)-oxo species can be written as the difference in energy of the C–H bond of the substrate that is broken with the O–H bond strength of the oxidant that is formed as described in Eq 6 – 8.[118-121] We calculate a BDE_{OH} value of ΔG = 86.5 kcal mol⁻¹ for the isolated iron(III)-hydroxo

9

complex. In combination with the BDE1$_{C2H}$ and BDE1$_{C3H}$ values of ΔG = 70.9 and 64.8 kcal mol^{-1}, respectively, give predicted driving forces for the first hydrogen atom abstraction step of ΔG = –15.6 and –21.7 kcal mol^{-1}. These predicted values are close to the Gibbs free energies of $^5IM_2$ and $^5IM_3$ shown in Figure 3 and hence, the overall hydrogen atom abstraction follows the strengths of the bonds that are broken and formed in the process.

$$Fe^{IV}(O) + Sub–H \rightarrow Fe^{III}(OH) + Sub^{\cdot} \qquad (6)$$

$$Fe^{III}(OH) \rightarrow Fe^{IV}(O) + H^{\cdot} + BDE_{OH} \qquad (7)$$

$$\Delta G_{Eq\,6} = BDE1_{CH} – BDE_{OH} \qquad (8)$$

Consequently based on the thermodynamics of hydrogen atom abstraction the most favorable pathway should be C^3–H activation of substrate by the iron(IV)-oxo oxidant. Indeed, the most stable radical intermediate is $^5IM_{3,\sigma}$, which is below $^5IM_{2,\sigma}$ by ΔG = 2.1 kcal mol^{-1}. However, as can be seen from Figure 3, the lowest hydrogen atom abstraction barrier is for hydrogen atom abstraction from the C^2–H bond rather than from the C^3–H bond. This implies that substrate positioning and activation does not follow the thermodynamically favorable and energetically expected pathway in flavonol synthase, but is guided by the second-coordination sphere of residues. As such, the enzyme preferentially abstracts a hydrogen atom from the strong C^2–H bond rather than the much weaker C^3–H bond.

The hydrogen atom abstraction steps via $^5TS1_{HA3,\sigma}$ and $^5TS1_{HA2,\sigma}$, by contrast, follow the reverse ordering of BDE1 values and consequently do not follow the Polanyi principle that links reaction exothermicity with barrier height or rate constant.[118-121] Thus, a systematic study of hydrogen atom abstraction reactions by iron(IV)-oxo complexes gave a linear correlation of the hydrogen atom abstraction barrier height with the BDE$_{CH}$ of the bond of the substrate that is broken during the process.[122-124] Clearly, the enzymatic reactivity differs from what would be expected in an ideal situation where substrate can approach the oxidant unperturbed. The second-coordination sphere effect and the substrate positioning clearly reverse the order of the barriers from the trend based on BDEs. In a similar vein, we recently showed that in prolyl-4-hydroxylase substrate and oxidant positioning guides the reaction to C^4–H hydroxylation even though C^5–H hydroxylation is thermodynamically favored.[90,125] It was shown that bulky aromatic residues, e.g. Tyr$_{140}$ and Trp$_{243}$ position the substrate through stereochemical repulsions of the aromatic groups as well as through hydrogen bonding interactions in the active site.
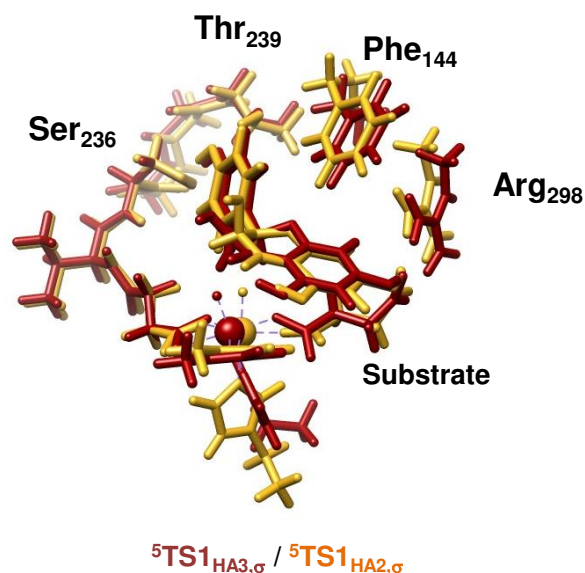
$^5TS1_{HA3,\sigma}$ / $^5TS1_{HA2,\sigma}$

	$^5TS1_{HA2,\sigma}$	$^5TS1_{HA3,\sigma}$
$\angle$C-H-O	178	157
$\angle$C-O-Fe	172	146
$\angle$O-Fe-N$_{His}$	176	177

Figure 6. Overlay of the optimized geometries of $^5TS1_{HA3,\sigma}$ (in wine red) and $^5TS1_{HA2,\sigma}$ (in amber) as obtained in Gaussian-09 at UB3LYP/BS1. Selected bond angles (in degrees) are given in the Table.

To understand the environmental effects of the protein, i.e. the second coordination sphere, on the rate determining transition states $^5TS1_{HA2,\sigma}$ and $^5TS1_{HA3,\sigma}$, we created an overlay of the two optimized transition state structures and display those in Figure 6. As can be seen most of the protein and oxidant atoms are in the same position in the two structures. This means that the structure is very rigid and most groups are linked together through strong hydrogen bonding interactions. The phenol group of the substrate is linked in hydrogen bonding interactions to the alcohol groups of the Ser$_{236}$ and Thr$_{239}$ amino acid side chains, whereas the resorcinol ring of the substrate is located above the succinate ligand of iron and hydrogen bonds to the salt bridge with the Arg$_{298}$ residue. These interactions anchor the substrate in position and position it with the C^2–C^3 bond adjacent to the iron(IV)-oxo species.
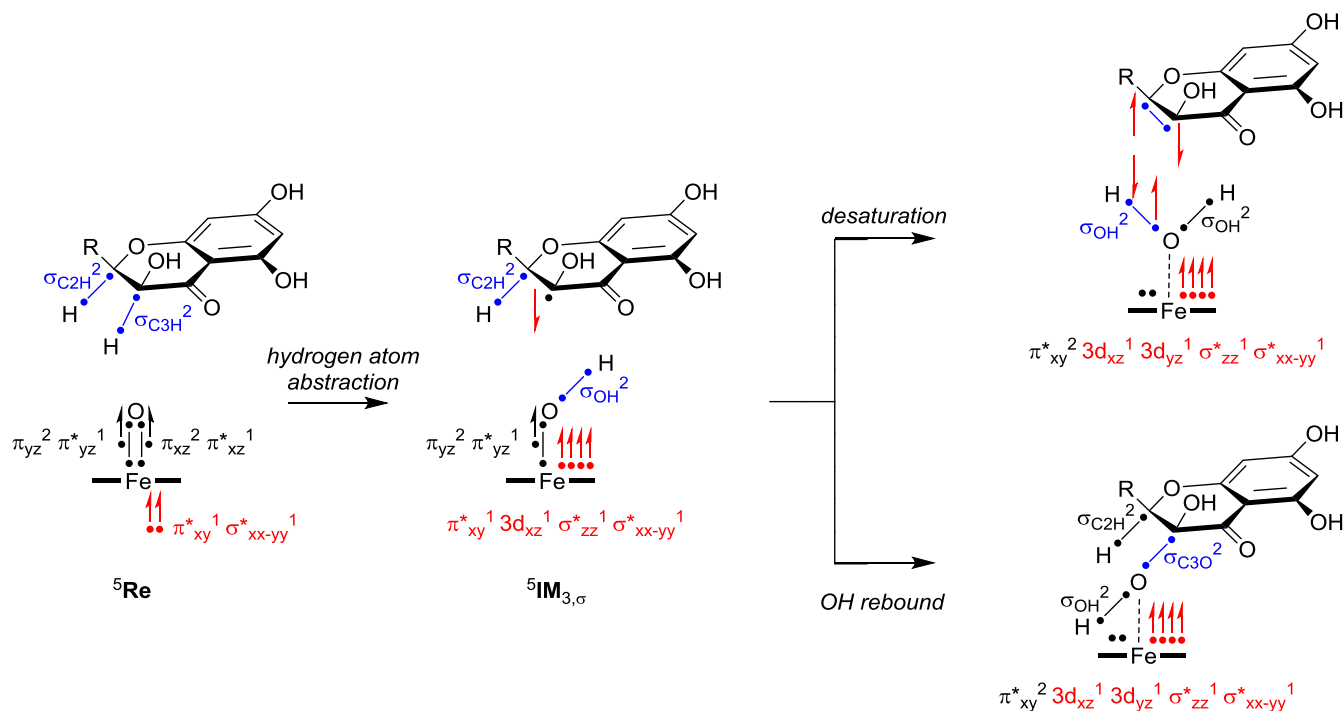
Figure 7. VB description of bonds that are broken and formed during the hydrogen atom abstraction and subsequent desaturation and OH rebound pathways. Valence electrons are identified with a dot and a line between two dots represents a doubly occupied orbital.

A detailed comparison of the two transition state structures $^5TS1_{HA2,\sigma}$ and $^5TS1_{HA3,\sigma}$ shows that the C–H bond is aligned to the Fe–O bond in $^5TS1_{HA2,\sigma}$ with an angle for the C-H-O group of 172°. By contrast in $^5TS1_{HA3,\sigma}$ the angle is considerably bent with a value of 146°, which implies there are considerable constraints on the hydrogen atom abstraction step. In addition, the C–O–Fe and O–Fe–N$_{His}$ angles are also close to linearity (172 and 176°, respectively) and hence the system is set-up for ideal electron transfer along a $^5\sigma$-pathway. Thus, in the $^5\sigma$-pathway an electron transfer takes place from the σ_{CH} bond of the substrate into the σ^*_{z2} orbital along the Fe–O axis. Often, therefore, $^5\sigma$-type transition states give an almost linear Fe–O–C angle,[105,106] as seen for $^5TS1_{HA2,\sigma}$.

However, in the C^3–H hydrogen atom abstraction transition state the angle is not under the ideal electronic and geometric conditions due to substrate positioning. In particular, there is a bent in the Fe–O–C^3 angle of 146°, but also the O–H–C angle has deviated from linearity at 157° and the O–H distance is elongated in the TS. The only other noticeable difference between the two transition state structures is a 90° rotation of the axial histidine ligand of iron.

These geometric differences and particularly the bending of the structure from the ideal linear angles for C–H–O, C–O–Fe and O–Fe–N$_{His}$ groups destabilize the $^5TS1_{HA3,\sigma}$ transition state structure and lift it above the transition state

for $^5TS1_{HA2,\sigma}$. Consequently, the enzyme abstracts the stronger C^2–H atom from substrate preferentially even though a weaker C^3–H bond is present nearby. But due to stereochemical constraints through substrate positioning and orientation, the oxidant does not have good access to this position.

To understand why the enzyme abstracts a hydrogen atom from the strongest one of the two C–H bonds first, we decided to investigate the reaction pathways leading to substrate desaturation and hydroxylation. Interestingly, the initial hydrogen atom abstraction from $^5TS1_{HA2,\sigma}$ is followed by a barrierless desaturation and a high energy rebound alternative cannot compete with this process. On the other hand for the pathway starting with C^3–H abstraction via $^5TS1_{HA3,\sigma}$ we find a stable radical intermediate that is followed by a relatively high second hydrogen atom abstraction barrier via $^5TS2_{HA3}$ that is $\Delta G^\ddagger = 11.5$ kcal mol^{-1} above the radical intermediate. The competitive radical rebound transition state for the formation of C^3–OH products is estimated to be 12 kcal mol^{-1} above the radical intermediate. Therefore, the pathway that passes $^5IM_2$ should lead to chemoselective desaturation, whereas a mixture of products is expected for the mechanism passing $^5IM_3$.

We designed a valence bond (VB) reaction scheme (Figure 7) to explain the electron transfer processes during the substrate desaturation and hydroxylation pathways as

11

started from the reactant configuration in the quintet spin state. As discussed above, the quintet spin reactant (^{5}Re) has an electronic configuration $\pi_{xz}^2 \pi_{yz}^2 \pi^{*1}_{xy} \pi^{*1}_{xz} \pi^{*1}_{yz} \sigma^{*1}_{z^2}$, whereby the π_{xz}/π^*_{xz} and π_{yz}/π^*_{yz} couples represent a two-center-three electron bond along the Fe–O bond. In Figure 7 the doubly occupied valence orbitals are given as a line separated by two dots, while the unpaired electrons are shown as a dot. In the hydrogen atom abstraction step, the σ-orbital for the C–H bond in the substrate (σ_{C3H}) breaks and splits back into atomic orbitals. One of those remains on the substrate as the radical (in π_{Sub}), while the second one pairs up with an electron on the oxo group to form the new σ_{OH} bond. In the process the two-center-three-electron π_{xz}/π^*_{xz} bond breaks and donates one electron into σ_{OH}, while the other two move into the $3d_{xz}$ and $\sigma^*_{x^2-y^2}$ orbitals.

Next, we explored the electronic differences for competitive OH rebound versus desaturation processes through a valence bond analysis of the orbitals. Thus, the radical intermediates ^{5}IM$_2$ and ^{5}IM$_3$ have an orbital occupation $\pi^{*1}_{xy} 3d^1_{xz} \pi_{yz}^2 \pi^{*1}_{yz} \sigma^{*1}_{z^2} \sigma^{*1}_{x^2-y^2}$. In the next stage of the reaction for both desaturation and hydroxylation, the $\pi_{yz}^2 \pi^{*1}_{yz}$ three-electron bond breaks as well and one of the electrons stays on oxygen, while the other two end up in the metal 3d-system in $3d_{yz}$ and π^*_{xy}. Therefore, both desaturation and hydroxylation steps will be dependent on the energy to break the $\pi_{yz}^2 \pi^{*1}_{yz}$ three-electron bond and the energy to promote an electron into the π^*_{xy} orbital, which we designate $E_{ex,FeOH}$. However, the electron that stays on oxygen either pairs up with the incoming hydrogen atom to form a new σ_{OH} orbital in the desaturation step or forms a σ_{CO} orbital by pairing up with the substrate radical in OH rebound. The energy differences of these bonds formed, i.e. the OH bond in water or the C–O bond in the alcohol will determine the relative energies of the desaturation versus rebound transition states.

Previously,[47,50] we established correlations that determine the rebound barrier ($\Delta E^{\ddagger}_{reb}$, Eq 9) and the desaturation barrier ($\Delta E^{\ddagger}_{desat}$, Eq 10) based on the molecular orbitals that are broken and formed in the process. The VB drawings in Figure 7 show the orbital and electron changes in the process from radical intermediate to desaturation and hydroxylation products. In the case of desaturation this is determined by the breaking of the $\pi_{yz}^2 \pi^{*1}_{yz}$ three-electron bond ($E_{ex,FeOH}$), the energy to break the σ_{CH} orbital of the substrate (E_{CH}), the energy to form the σ_{OH} orbital in the iron(II)-water complex (E_{OH}) and the energy to form new π-bond in the product (E_π). On the other hand, the OH rebound barrier is dependent on the energy to break the $\pi_{yz}^2 \pi^{*1}_{yz}$ three-electron bond ($E_{ex,FeOH}$) and the strength of the σ_{CO} orbital that is formed (E_{CO}).

$$\Delta E^{\ddagger}_{reb} \approx (E_{ex,FeOH} - E_{CO})/3 \qquad (9)$$

$$\Delta E^{\ddagger}_{desat} \approx (E_{CH} - E_{OH} + E_{ex,FeOH} - E_\pi)/3 \qquad (10)$$

We estimated values for each of the contributions in Eq 9 and 10 based on the orbital energies in the radical intermediates and the isolated product complexes. The energy of the π-bond in the substrate that is formed was estimated from the singlet-triplet energy gap in the product flavonol as $E_{\pi,2}$ = 50.2 kcal mol^{-1} for the pathway from ^{5}IM$_{2,\sigma}$, while it is $E_{\pi,3}$ = 31.4 kcal mol^{-1} for the pathway from ^{5}IM$_{3,\sigma}$. The difference between the two values comes from a large geometric change for the desaturation from the C^3-radical and the rearrangement energy was included in the E_π value. Subsequently, we calculated adiabatic BDE values for the strength of the C–H bond in the radical intermediate (BDE$_2$) and find energies of cleavage of the C^3–H bond in the radical on C^2 as E_{C3-H} = 34.0 kcal mol^{-1}, while the strength of the C^2–H bond in the structure with a radical on C^3 is E_{C2-H} = 40.5 kcal mol^{-1}. Next, we calculated the strength of the C–O bond of the alcohol that is formed (BDE$_{CO}$), from the energy difference of the alcohol minus that of the radical and an isolated OH radical. Values for the strength of the C^2–OH and C^3–OH bonds are E_{C2-O} = 79.0 and E_{C3-O} = 73.0 kcal mol^{-1}, respectively. In addition, we calculated the strength of the O–H bond in the Fe(II)(H$_2$O) complex and obtained a value of E_{OH} = 85.2 kcal mol^{-1}, respectively. Finally, the orbital rearrangement for the breaking of the π_{yz}/π^*_{yz} bond was estimated from the molecular orbitals in ^{5}IM$_2$ and ^{5}IM$_3$ as $E_{ex,FeOH,2}$ = 95.8 kcal mol^{-1} and $E_{ex,FeOH,3}$ = 102.9 kcal mol^{-1}.

$$\Delta E^{\ddagger}_{VB,reb,C2} \approx (E_{ex,FeOH,2} - E_{C2-O})/3 \qquad (11)$$

$$\Delta E^{\ddagger}_{VB,desat,C3} \approx (E_{C3-H} - E_{OH} + E_{ex,FeOH,2} - E_{\pi,2})/3 \qquad (12)$$

$$\Delta E^{\ddagger}_{VB,reb,C3} \approx (E_{ex,FeOH,3} - E_{C3-O})/3 \qquad (13)$$

$$\Delta E^{\ddagger}_{VB,desat,C2} \approx (E_{C2-H} - E_{OH} + E_{ex,FeOH,3} - E_{\pi,3})/3 \qquad (14)$$

The VB estimated barriers heights for OH rebound and desaturation processes from ^{5}IM$_{2,\sigma}$ and ^{5}IM$_{3,\sigma}$ were calculated from the bond strengths of the orbitals broken and formed in the processes (Eqs 11 – 14) and are summarized in Figure 8. The pathway from ^{5}IM$_{2,\sigma}$ has a barrierless desaturation and an OH rebound barrier of $\Delta E^{\ddagger}_{VB,reb3}$ = 5.6 kcal mol^{-1}. This implies that the pathway via ^{5}IM$_{2,\sigma}$ will give dominant desaturation and little hydroxylation. By contrast, the pathway through ^{5}IM$_{3,\sigma}$ gives a rebound barrier of $\Delta E^{\ddagger}_{VB,reb2}$ = 10.0 kcal mol^{-1} and a desaturation barrier of $\Delta E^{\ddagger}_{VB,desat,C3}$ = 8.9 kcal mol^{-1}. As such the two barriers are

close in energy and the processes competitive. Consequently, the VB modelling predicts regioselective desaturation via $^5IM_{2,\sigma}$, whereas a mixture of products from desaturation and hydroxylation is expected via $^5IM_{3,\sigma}$. The reason for this is that the desaturation pathway via $^5IM_{3,\sigma}$ is destabilized due to a stronger C–H bond that needs to be broken, but also due to geometric changes in the FeOH group (see overlay in Figure 6 above) the strength of the FeOH interaction has increased. On the other hand, the bond strength of the C^3–OH interaction is larger than that of the C^2–OH one, but not large enough to overcome the difference in desaturation between the two pathways.
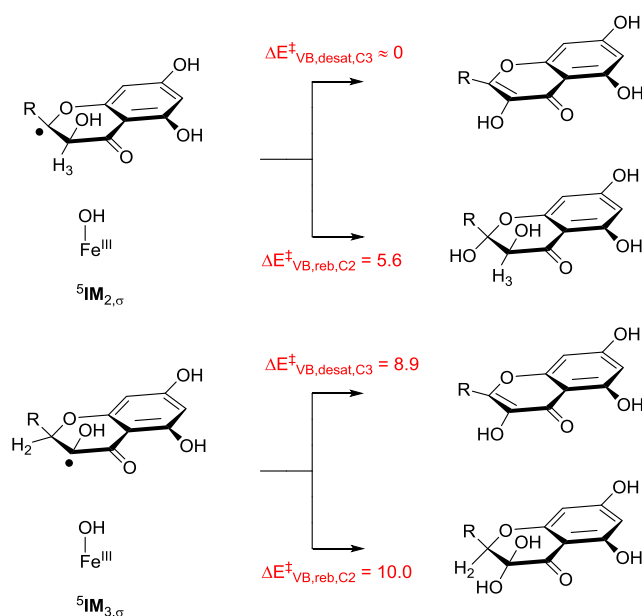

Figure 8. Estimated rebound and desaturation barriers from $^5IM_{2,\sigma}$ and $^5IM_{3,\sigma}$ from VB with values in kcal mol^{-1}.

Thus, the DFT calculations presented in this work show that the hydrogen atom from the strong C^2–H bond is abstracted first rather than from the weaker C^3–H bond. As a consequence, the desaturation step, i.e. the second hydrogen atom abstraction, will come from the cleavage of a much weaker C–H bond. That means the radical intermediate will have a short lifetime and react to desaturation products rapidly; thereby, avoiding reaction pathways leading to by-products such as OH rebound to form alcohols. Therefore, it may very well be that the enzyme was designed in such a way that the substrate is positioned with the C^2–H bond closest to the iron center to trigger an initial C^2–H hydrogen atom abstraction and deliver a chemoselective substrate desaturation reaction with limited by-products. Indeed, our DFT calculations show a competitive substrate hydroxylation pathway from $^5IM_{3,\sigma}$ alongside a high-energy second hydrogen atom abstraction reaction.

CONCLUSION.

In this work a DFT study on the mechanism of flavonol synthase enzymes is described. We show that the desaturation reaction is triggered by a rate-determining hydrogen atom abstraction step from the strongest of the two C–H bonds in the substrate. This is achieved through careful substrate positioning in the active site and locking it in place with strong hydrogen bonding interactions. The reaction is followed by abstraction of a much weaker C–H bond that leads to rapid formation of the desaturated product. By contrast, had the reaction taken place with abstraction of the weaker C–H bond first then considerable amount of hydroxylated product would have been obtained. Therefore, substrate and oxidant positioning is an important feature in nonheme iron dioxygenases that guides the substrate selectivity.

ASSOCIATED CONTENT

Supporting Information. Computational data, including absolute and relative energies, group spin densities and charges, constraint geometry scans, optimized geometries and intrinsic reaction coordinate scans as well as a full set of Cartesian coordinates of optimized geometries is available. This material is available free of charge via the Internet at http://pubs.acs.org.

AUTHOR INFORMATION

Corresponding Author

* sam.devisser@manchester.ac.uk (SdV).

Author Contributions

The manuscript was written through contributions of all authors.

ACKNOWLEDGMENT

ABBREVIATIONS

DFT, density functional theory; ZPE, zero-point energy; TS, transition state; FHT, flavanone-3β-hydroxylase; FLS, flavonol synthase; TauD, taurine/α-ketoglutarate dioxygenase; EPR, electron paramagnetic resonance; BDE, bond dissociation free energy; VB, valence bond.

REFERENCES

(1)   Sono, M.; Roach, M. P.; Coulter, E. D.; Dawson, J. H. Heme-containing oxygenases. *Chem. Rev.* 1996, *96*, 2841–2888.

(2)   Meunier, B.; de Visser, S. P.; Shaik, S. Mechanism of oxidation reactions catalyzed by cytochrome P450 enzymes. *Chem. Rev.* 2004, *104*, 3947–3980.

(3) Denisov, I. G.; Makris, T. M.; Sligar, S. G.; Schlichting, I. Structure and chemistry of cytochrome P450. *Chem. Rev.* 2005, *105*, 2253–2277.

(4) Ortiz de Montellano, P. R., Ed., *Cytochrome P450: Structure, Mechanism and Biochemistry*, 3rd ed., Kluwer Academic/Plenum Publishers, New York, 2005.

(5) Ortiz de Montellano, P. R. Hydrocarbon hydroxylation by cytochrome P450 enzymes. *Chem. Rev.* 2010, *110*, 932–948.

(6) Grogan, G. Cytochromes P450: Exploiting diversity and enabling application as biocatalysts. *Curr. Opin. Chem. Biol.* 2011, *15*, 241–248.

(7) Fasan, R. Tuning P450 enzymes as oxidation catalysts. *ACS Catal.* 2012, *2*, 647–666.

(8) Poulos, T. L. Heme enzyme structure and function. *Chem. Rev.* 2014, *114*, 3919–3962.

(9) Huang, X.; Groves, J. T. Oxygen activation and radical transformations in heme proteins and metalloporphyrins. *Chem. Rev.* 2018, *118*, 2491–2553.

(10) de Visser, S. P.; Kumar, D. (Eds.) *Iron-containing enzymes: Versatile catalysts of hydroxylation reactions in nature*, Royal Society of Chemistry Publishing, Cambridge (UK), 2011.

(11) Que Jr, L. One motif—many different reactions. *Nat. Struct. Biol.* 2000, *7*, 182–184.

(12) Kovaleva, E. G.; Lipscomb, J. D. Versatility of biological non-heme Fe(II) centers in oxygen activation reactions. *Nat. Chem. Biol.* 2008, *4*, 186–193.

(13) Bruijnincx, P. C. A.; van Koten, G.; Klein Gebbink, R. J. M. Mononuclear non-heme iron enzymes with the 2-His-1-carboxylate facial triad: recent developments in enzymology and modeling studies. *Chem. Soc. Rev.* 2008, *37*, 2716–2744.

(14) Solomon, E. I.; Brunold, T. C.; Davis, M. I.; Kemsley, J. N.; Lee, S. K.; Lehnert, N.; Neese, F.; Skulan, A. J.; Yang, Y. S.; Zhou, J. Geometric and electronic structure/function correlations in non-heme iron enzymes. *Chem. Rev.* 2000, *100*, 235–349.

(15) Costas, M.; Mehn, M. P.; Jensen, M. P.; Que Jr., L. Dioxygen activation at mononuclear nonheme iron active sites: Enzymes, models, and intermediates. *Chem. Rev.* 2004, *104*, 939–986.

(16) Abu-Omar, M. M.; Loaiza, A.; Hontzeas, N. Reaction mechanisms of mononuclear non-heme iron oxygenases. *Chem. Rev.* 2005, *105*, 2227–2252.

(17) McDonald, A. R.; Que Jr, L. High-valent nonheme iron-oxo complexes: Synthesis, structure, and spectroscopy. *Coord. Chem. Rev.* 2013, *257*, 414–428.

(18) Nam, W.; Lee, Y.-M.; Fukuzumi, S. Tuning reactivity and mechanism in oxidation reactions by mononuclear nonheme iron(IV)-oxo complexes. *Acc. Chem. Res.* 2014, *47*, 1146–1154.

(19) Stipanuk, M. H. Sulfur Amino Acid Metabolism: Pathways for production and removal of homocysteine and cysteine. *Annu. Rev. Nutr.* 2004, *24*, 539–577.

(20) Straganz, G. D.; Nidetzky, B. Variations of the 2-His-1-carboxylate theme in mononuclear non-heme Fe^{II} oxygenases. *ChemBioChem.* 2006, *7*, 1536–1548.

(21) Joseph, C. A.; Maroney, M. J. Cysteine dioxygenase: structure and mechanism. *Chem. Commun.* 2007, 3338–3349.

(22) Buongiorno, D.; Straganz, G. D. Structure and function of atypically coordinated enzymatic mononuclear non-heme-Fe(II) centers. *Coord. Chem. Rev.* 2013, *257*, 541–563.

(23) Tchesnokov, E. P.; Fellner, M.; Siakkou, E.; Kleffmann, T.; Martin, L. W.; Aloi, S.; Lamont, I. L.; Wilbanks, S. M.; Jameson, G. N. L. The cysteine dioxygenase homologue from *Pseudomonas aeruginosa* is a 3-mercaptopropionate dioxygenase. *J. Biol. Chem.* 2015, *290*, 24424–24437.

(24) McDonough, M. A.; Li, V.; Flashman, E.; Chowdhury, R.; Mohr, C.; Lienard, B. M.; Zondlo, J.; Oldham, N. J.; Clifton, I. J.; Lewis, J.; McNeill, L. A.; Kurzeja, R. J.; Hewitson, K. S.; Yang, E.; Jordan, S.; Syed, R. S.; Schofield, C. J. Cellular oxygen sensing: Crystal structure of hypoxia-inducible factor prolyl hydroxylase (PHD2). *Proc. Natl. Acad. Sci. USA* 2006, *103*, 9814–9819.

(25) Koski, M. K.; Hieta, R.; Hirsilä, M.; Rönkä, A.; Myllyharju, J.; Wierenga, R. K. The crystal structure of an algal prolyl 4-hydroxylase complexed with a proline-rich peptide reveals a novel buried tripeptide binding motif. *J. Biol. Chem.* 2009, *284*, 25290–25301.

(26) Schofield, C. J.; Zhang, Z. Structural and mechanistic studies on 2-oxoglutarate-dependent oxygenases and related enzymes. *Curr. Opin. Struc. Biol.* 1999, *9*, 722–731.

(27) O'Brien, P. J. Catalytic promiscuity and the divergent evolution of DNA repair enzymes. *Chem. Rev.* 2006, *106*, 720–752.

(28) Yi, C.; Yang, C. G.; He, C. A Non-heme iron-mediated chemical demethylation in DNA and RNA. *Acc. Chem. Res.* 2009, *42*, 519–529.

(29) de Visser, S. P. Mechanistic insight on the activity and substrate selectivity of nonheme iron dioxygenases. *Chem. Record* 2018, *18*, 1501–1516.

(30) Proshlyakov, D. A.; Henshaw, T. F.; Monterosso, G. R.; Ryle, M. J.; Hausinger, R. P. Direct detection of oxygen intermediates in the non-heme Fe enzyme taurine/α-ketoglutarate dioxygenase. *J. Am. Chem. Soc.* 2004, *126*, 1022–1023.

(31) Bollinger Jr, J. M.; Price, J. C.; Hoffart, L. M.; Barr, E. W.; Krebs, C. Mechanism of taurine: α-ketoglutarate dioxygenase (TauD) from *Escherichia coli. Eur. J. Inorg. Chem.* 2005, 4245–4254.

(32) Ray, K.; Pfaff, F. F.; Wang, B.; Nam, W. Status of Reactive non-heme metal–oxygen intermediates in chemical and enzymatic reactions. *J. Am. Chem. Soc.* 2014, *136*, 13942–13958.

(33) Brisson, L.; El Bakkali-Taheri, N.; Giorgi, M.; Fadel, A.; Kaizer, J.; Réglier, M.; Tron, T.; Ajandouz, E. H.; Simaan, A. J. 1-Aminocyclopropane-1-carboxylic acid oxidase: insight into cofactor binding from experimental and theoretical studies. *J. Biol. Inorg. Chem.* 2012, *17*, 939–949.

(34) White, M. D.; Flashman, E. Catalytic strategies of the non-heme iron dependent oxygenases and their roles in plant biology. *Curr. Opin. Chem. Biol.* 2016, *31*, 126–135.

(35) Li, C.; Liu, S.; Yao, X.; Wang, J.; Wang, T.; Zhang, Z.; Zhang, P.; Chen, K. Effects of 2,4-epibrassinolide on photosynthesis and Rubisco activase gene expression in *Triticum aestivum L.* seedlings under a combination of drought and heat stress. *Plant Growth Regul.* 2017, *83*, 489–500.

(36) Wexler, S.; Schayek, H.; Rajendar, K.; Tal, I.; Shani, E.; Meroz, Y.; Dobrovetsky, R.; Weinstain, R. Characterizing gibberellin flow in planta using photocaged gibberellins. *Chem. Sci.* 2019, *10*, 1500–1505.

(37) Honda, C.; Kotoda, N.; Wada, M.; Kondo, S.; Kobayashi, S.; Soejima, J.; Zhang, Z.; Tsuda, T.; Moriguchi, t. Anthocyanin biosynthetic genes are coordinately expressed during red

coloration in apple skin. *Plant Physiol. Biochem.* 2002, *40*, 955–962.

(38)   Martens, S.; Preuß, A.; Matern, U. Multifunctional flavonoid dioxygenases: Flavonol and anthocyanin biosynthesis in *Arabidopsis thaliana L. Phytochemistry* 2010, *71*, 1040–1049.

(39)   Song, J.; Du, L.; Li, L.; Kalt, W.; Campbell Palmer, L.; Fillmore, S.; Zhang, Y.; Zhang, Z. Q.; Li, X. H. Quantitative changes in proteins responsible for flavonoid and anthocyanin biosynthesis in strawberry fruit at different ripening stages: A targeted quantitative proteomic investigation employing multiple reaction monitoring. *J. Proteomics* 2015, *122*, 1–10.

(40)   Liu, M.; Li, X.; Liu, Y.; Cao, B. Regulation of flavanone 3-hydroxylase gene involved in the flavonoid biosynthesis pathway in response to UV-B radiation and drought stress in the desert plant, *Reaumuria soongorica. Plant Physiol. Biochem.* 2013, *73*, 161–167.

(41)   Li, C.; Liu, S.; Yao, X.; Wang, J.; Wang, T.; Zhang, Z.; Zhang, P.; Chen, K. PnF3H, a flavanone 3-hydroxylase from the Antarctic moss *Pohlia nutans*, confers tolerance to salt stress and ABA treatment in transgenic *Arabidopsis. Plant Growth Regul.* 2017, *83*, 489–500.

(42)   Zeb, N.; Rashid, M. H.; Mubarak, M. Q. E.; Ghafoor, S.;. de Visser, S. P. Flavonol biosynthesis by nonheme iron dioxygenases: A computational study into the structure and mechanism. *J. Inorg. Biochem.* 2019, *198*, 110728.

(43)   Aik, W. S.; Chowdhury, R.; Clifton, I. J.; Hopkinson, R. J.; Leissing, T.; McDonough, M. A.; Nowak, R.; Schofield, C. J.; Walport, L. J. *Introduction to structural studies on 2-oxoglutarate-dependent oxygenases and related enzymes*. In *RSC Metallobiology Series* No. 3, Eds: Hausinger, R. P.; Schofield C. J. (Eds.), Royal Society of Chemistry, Cambridge (UK), 2015, Chapter 2, pp 59–94.

(44)   Welford, R. W. D.; Clifton, I. J.; Turnbull, J. J.; Wilson, S. C.; Schofield, C. J. Structural and mechanistic studies on anthocyanidin synthase catalysed oxidation of flavanone substrates: the effect of C-2 stereochemistry on product selectivity and mechanism. *Org. Biomol. Chem.* 2005, *3*, 3117–3126.

(45)   Shaik, S.; Cohen, S.; de Visser, S. P.; Sharma, P. K.; Kumar, D.; Kozuch, S.; Ogliaro, F.; Danovich, D. The "rebound controversy": An overview and theoretical modeling of the rebound step in C–H hydroxylation by cytochrome P450. *Eur. J. Inorg. Chem.* 2004, 207–226.

(46)   Li, X.-X.; Postils, V.; Sun, W.; Faponle, A. S.; Solà, M.; Wang, Y.; Nam, W.; de Visser, S. P. Reactivity patterns of (protonated) Compound II and Compound I of Cytochrome P450: Which is the better oxidant? *Chem. Eur. J.* 2017, *23*, 6406–6418.

(47)   Ji, L.; Faponle, A. S.; Quesne, M. G.; Sainna, M. A.; Zhang, J.; Franke, A.; Kumar, D.; van Eldik, R.; Liu, W.; de Visser, S. P. Drug metabolism by cytochrome P450 enzymes: What distinguishes the pathways leading to substrate hydroxylation over desaturation? *Chem. Eur. J.* 2015, *21*, 9083–9092.

(48)   Berman, H. M.; Westbrook, J.; Feng, Z.; Gilliland, G.; Bhat, T. N.; Weissig, H.; Shindyalov, I. N.; Bourne, P. E. The Protein Data Bank. *Nucl. Acids Res.* 2000, *28*, 235–242.

(49)   Quesne, M. G.; Borowski, T.; de Visser, S. P. Quantum mechanics/molecular mechanics modelling of enzymatic processes: Caveats and breakthroughs. *Chem. Eur. J.* 2016, *22*, 2562–2581.

(50)   Faponle, A. S.; Quesne, M. G.; de Visser, S. P. Origin of the regioselective fatty acid hydroxylation versus decarboxyla-

tion by a cytochrome P450 peroxygenase: What drives the reaction to biofuel production? *Chem. Eur. J.* 2016, *22*, 5478–5483.

(51)   Faponle, A. S.; Seebeck, F. P.; de Visser, S. P. Sulfoxide synthase versus cysteine dioxygenase reactivity in a nonheme iron enzyme. *J. Am. Chem. Soc.* 2017, *139*, 9259–9270.

(52)   Grosdidier, A.; Zoete, V.; Michielin, O. SwissDock, a Protein-Small Molecule Docking Web Service Based on EADock DSS. *Nucl. Acids Res.* 2011, *39*, W270–277.

(53)   Pettersen, E. F.; Goddard, T. D.; Huang, C. C.; Couch, G. S.; Greenblatt, D. M.; Meng, E. C.; Ferrin, T. E. UCSF Chimera--a visualization system for exploratory research and analysis. *J. Comput. Chem.* 2004, *25*, 1605-1612.

(54)   *Gaussian*-09, Revision C.01, Frisch, M. J.; Trucks, G. W.; Schlegel, H. B.; Scuseria, G. E.; Robb, M. A.; Cheeseman, J. R.; Scalmani, G.; Barone, V.; Mennucci, B.; Petersson, G. A.; Nakatsuji, H.; Carica-to, M.; Li, X.; Hratchian, H. P.; Izmaylov, A. F.; Bloino, J.; Zheng, G.; Sonnenberg, J. L.; Hada, M.; Ehara, M.; Toyota, K.; Fukuda, R.; Hasegawa, J.; Ishida, M.; Nakajima, T.; Honda, Y.; Kitao, O.; Nakai, H.; Vreven, T.; Montgomery Jr, J. A.; Peralta, J. E.; Ogliaro, F.; Bearpark, M.; Heyd, J. J.; Brothers, E.; Kudin, K. N.; Staroverov, V. N.; Keith, T.; Kobayashi, R.; Normand, J.; Raghavachari, K.; Rendell, A.; Burant, J. C.; Iyengar, S. S.; Tomasi, J.; Cossi, M.; Rega, N.;. Millam, J. M.; Klene, M.; Knox, J. E.; Cross, J. B.; Bakken, V.; Adamo, C.; Jaramillo, J.; Gomperts, R.; Stratmann, R. E.; Yazyev, O.; Austin, A. J.; Cammi, R.; Pomelli, C.; Ochterski, J. W.; Martin, R. L.; Morokuma, K.;. Zakrzewski, V. G.; Voth, G. A.; Salvador, P.; Dannenberg, J. J.; Dapprich, S.; Daniels, A. D.; Farkas, O.; Foresman, J. B.; Ortiz, J. V.; Cioslowski, J.; Fox, D. J. Gaussian, Inc., Wallingford CT, 2013.

(55)   Becke, A. D. Density-Functional Thermochemistry. III. The Role of Exact Exchange. *J. Chem. Phys.* 1993, *98*, 5648–5652.

(56)   Lee, C.; Yang, W.; Parr, R. G. Development of the Colle-Salvetti Correlation-Energy Formula into a Functional of the Electron Density. *Phys. Rev. B* 1988, *37*, 785–789.

(57)   Hay, P. J.; Wadt, W. R. Ab Initio effective core potentials for molecular calculations. Potentials for the transition metal atoms Sc to Hg. *J. Chem. Phys.* 1985, *82*, 270–283.

(58)   Ditchfield, R.; Hehre, W. J.; Pople, J. A. Self-consistent molecular-orbital methods. IX. An extended Gaussian-type basis for molecular-orbital studies of organic molecules. *J. Chem. Phys.* 1971, *54*, 724–728.

(59)   Francl, M. M.; Pietro, W. J.; Hehre, W. J.; Binkley, J. S.; Gordon, M. S.; DeFrees, D. J.; Pople, J. A. Self-consistent molecular orbital methods. XXIII. A polarization-type basis set for second-row elements. *J. Chem. Phys.* 1982, *77*, 3654–3658.

(60)   Tomasi, J.; Mennucci, B.; Cammi, R. Quantum mechanical continuum solvation models. *Chem. Rev.* 2005, *105*, 2999–3093.

(61)   Cantú Reinhard, F. G.; Faponle, A. S.; de Visser, S. P. Substrate sulfoxidation by an iron(IV)-oxo complex: benchmarking computationally calculated barrier heights to experiment. *J. Phys. Chem. A* 2016, *120*, 9805–9814.

(62)   Cantú Reinhard, F. G.; Barman, P.; Mukherjee, G.; Kumar, J.; Kumar, D.; Kumar, D.; Sastri, C. V.; de Visser, S. P. Keto-enol tautomerization triggers an electrophilic aldehyde deformylation reaction by a nonheme manganese(III)-peroxo complex. *J. Am. Chem. Soc.* 2017, *139*, 18328–18338.

(63) Pickl, M.; Kurakin, S.; Cantú Reinhard, F. G.; Schmid, P.; Pöcheim, A.; Winkler, C. K.; Kroutil, W.; de Visser, S. P.; Faber, K. Mechanistic studies of fatty acid activation by CYP152 peroxygenases reveal unexpected desaturase activity. *ACS Catal.* 2019, *9*, 565–577.

(64) Grimme, S.; Antony, J.; Ehrlich, S.; Krieg, H. A Consistent and accurate ab initio parametrization of density functional dispersion correction (DFT-D) for the 94 elements H-Pu. *J. Chem. Phys.* 2010, *132*, 154104.

(65) Bigeleisen, J.; Wolfsberg, M. Theoretical and experimental aspects of isotope effects in chemical kinetics. In Advance in Chemical Physics, Prigogine, I. (Ed.); 1958, Volume I, pp 15–76.

(66) Heyes, D. J.; Sakuma, M.; de Visser, S. P.; Scrutton, N. S. Nuclear quantum tunneling in the light-activated enzyme protochlorophyllide oxidoreductase. *J. Biol. Chem.* 2009, *284*, 3762–3767.

(67) Barman, P.; Upadhyay, P.; Faponle, A. S.; Kumar, J.; Nag, S. S.; Kumar, D.; Sastri, C. V.; de Visser, S. P. Deformylation reaction by a nonheme manganese(III)-peroxo complex via initial hydrogen atom abstraction. *Angew. Chem. Int. Ed.* 2016, *55*, 11091–11095.

(68) Borowski, T.; Bassan, A.; Siegbahn, P. E. M. Mechanism of dioxygen activation in 2-oxoglutarate-dependent enzymes: A hybrid DFT study. *Chem. Eur. J.* 2004, *10*, 1031–1041.

(69) de Visser, S. P. Can the peroxosuccinate complex in the catalytic cycle of taurine/α-ketoglutarate dioxygenase (TauD) act as an alternative oxidant? *Chem. Commun.* 2007, 171–173.

(70) Nemukhin, A. V.; Topol, I. A.; Cachau, R. E.; Burt, S. K. On the nature of oxoiron (IV) intermediate in dioxygen activation by non-heme enzymes. *Theor. Chem. Acc.* 2006, *115*, 348–353.

(71) Sinnecker, S.; Svensen, N.; Barr, E. W.; Ye, S.; Bollinger Jr, J. M.; Neese, F.; Krebs, C. Spectroscopic and computational evaluation of the structure of the high-spin Fe(IV)-oxo intermediates in taurine: α-ketoglutarate dioxygenase from *Escherichia coli* and its His99Ala ligand variant. *J. Am. Chem. Soc.* 2007, *129*, 6168–6179.

(72) Chen, H.; Lai, W.; Yao, J.; Shaik, S. Perferryl Fe^V–oxo nonheme complexes: Do they have high-spin or low-spin ground states? *J. Chem. Theory Comput.* 2011, *7*, 3049–3053.

(73) Bushnell, E. A. C.; Fortowsky, G. B.; Gauld, J. W. Model iron–oxo species and the oxidation of imidazole: Insights into the mechanism of OvoA and EgtB? *Inorg. Chem.* 2012, *51*, 13351–13356.

(74) Wójcik, A.; Radoń, M.; Borowski, T. Mechanism of O2 activation by α-ketoglutarate dependent oxygenases revisited. A quantum chemical study. *J. Phys. Chem. A* 2016, *120*, 1261–1274

(75) Blomberg, M. R. A.; Borowski, T.; Himo, F.; Liao, R.-Z.; Siegbahn, P. E. M. Quantum chemical studies of mechanisms for metalloenzymes. *Chem. Rev.* 2014, *114*, 3601–3658.

(76) Song, X.; Lu, J.; Lai, W. Mechanistic insights into dioxygen activation, oxygen atom exchange and substrate epoxidation by AsqJ dioxygenase from quantum mechanical/molecular mechanical calculations. *Phys. Chem. Chem. Phys.* 2017, *19*, 20188-20197.

(77) Su, H.; Sheng, X.; Zhu, W.; Ma, G.; Liu, Y. Mechanistic insights into the decoupled desaturation and epoxidation catalyzed by dioxygenase AsqJ involved in the biosynthesis of quinolone alkaloids. *ACS Catal.* 2017, *7*, 5534-5543.

(78) Álvarez-Barcia, S.; Kästner, J. Atom tunneling in the hydroxylation process of taurine/α-ketoglutarate dioxygenase identified by quantum mechanics/molecular mechanics simulations. *J. Phys. Chem. B* 2017, *121*, 5347-5354.

(79) Yu, C.-P.; Tang, Y.; Cha, L.; Milikisiyants, S.; Smirnova, T. I.; Smirnov, A. I.; Guo, Y.; Chang, W.-c. Elucidating the reaction pathway of decarboxylation-assisted olefination catalyzed by a mononuclear Non-heme iron enzyme. *J. Am. Chem. Soc.* 2018, *140*, 15190-15193.

(80) Manna, R. N.; Malakar, T.; Jana, B.; Paul, A. Unraveling the crucial role of single active water molecule in the oxidative cleavage of aliphatic C–C bond of 2,4'-dihydroxy acetophenone Catalyzed by 2,4'-Dihydroxyacetophenone dioxygenase enzyme: A quantum mechanics/molecular mechanics investigation. *ACS Catal.* 2018, *8*, 10043-10050.

(81) Iyer, S. R.; Chaplin, V. D.; Knapp, M. J.; Solomon, E. I. O$_2$ activation by nonheme Fe^{II} α-ketoglutarate-dependent enzyme variants: Elucidating the role of the facial triad carboxylate in FIH. *J. Am. Chem. Soc.* 2018, *140*, 11777-11783.

(82) Dunham, N. P.; Chang, W.-c.; Mitchell, A. J.; Martinie, R. J.; Zhang, B.; Bergman, J. A.; Rajakovich, L. J.; Wang, B.; Boal, A. K.; Bollinger Jr, J. M. Two distinct mechanisms for C–C desaturation by iron(II)- and 2-(oxo)glutarate-dependent oxygenases: Importance of α-heteroatom assistance. *J. Am. Chem. Soc.* 2018, *140*, 7116-7126.

(83) Xue, J.; Lu, J.; Lai, W. Mechanistic insights into the non-heme 2-oxoglutarate-dependent ethylene-forming enzyme: Selectivity of ethylene-formation versus L-Arg hydroxylation. *Phys. Chem. Chem. Phys.* 2019, *21*, 9957-9968.

(84) Nakajima, J.-i.; Sato, Y.; Hoshino, T.; Yamazaki, M.; Saito, K. Mechanistic study on the oxidation of anthocyanidin synthase by quantum mechanical calculation. *J. Biol. Chem.* 2006, *281*, 21387-21398.

(85) Price, J. C.; Barr, E. W.; Tirupati, B.; Bollinger Jr, J. M.; Krebs, C. The first direct characterization of a high-valent iron intermediate in the reaction of an α-ketoglutarate-dependent dioxygenase: A high-spin Fe(IV) complex in taurine/α-ketoglutarate dioxygenase (TauD) from *Escherichia coli. Biochemistry* 2003, *42*, 7497-7508.

(86) Riggs-Gelasco, P. J.; Price, J. C.; Guyer, R. B.; Brehm, J. H.; Barr, E. W.; Bollinger Jr, J. M.; Krebs, C. EXAFS spectroscopic evidence for an Fe=O unit in the Fe(IV) intermediate observed during oxygen activation by taurine:α-ketoglutarate dioxygenase. *J. Am. Chem. Soc.* 2004, *126*, 8108-8109.

(87) Yan, W.; Song, H.; Song, F.; Guo, Y.; Wu, C.-H.; Her, A. S.; Pu, Y.; Wang, S.; Naowarojna, N.; Weitz, A.; Hendrich, M. P.; Costello, C. E.; Zhang, L.; Liu, P.; Zhang, Y. J. Endoperoxide formation by an α-ketoglutarate dependent mononuclear non-haem iron enzyme. *Nature* 2015, *527*, 539-543.

(88) Galonić Fujimori, D.; Barr, E. W.; Matthews, M. L.; Koch, G. M.; Yonce, J. R.; Walsh, C. T.; Bollinger, Jr., J. M.; Krebs, C.; Riggs-Gelasco, P. J. Spectroscopic evidence for a high-spin Br-Fe(IV)-Oxo Intermediate in the α-ketoglutarate-dependent halogenase CytC3 from *Streptomyces. J. Am. Chem. Soc.* 2007, *129*, 13408-13409.

(89) Godfrey, E.; Porro, C. S.; de Visser, S. P. Comparative quantum mechanics / molecular mechanics (QM/MM) and density functional theory calculations on the oxo-iron species of taurine/α-ketoglutarate dioxygenase. *J. Phys. Chem. A* 2008, *112*, 2464-2468.

(90) Karamzadeh, B.; Kumar, D.; Sastry, G. N.; de Visser, S. P. Steric factors override thermodynamic driving force in regioselectivity of proline hydroxylation by prolyl-4-hydroxylase enzymes. *J. Phys. Chem. A* 2010, *114*, 13234–13243.

(91) de Visser, S. P. Differences in and comparison of the catalytic properties of heme and non-heme enzymes with a central oxo-iron group. *Angew. Chem. Int. Ed.* 2006, *45*, 1790–1793.

(92) Latifi, R.; Sainna, M. A.; Rybak-Akimova, E. V.; de Visser, S. P. Does hydrogen-bonding donation to manganese(IV)-oxo and iron(IV)–oxo oxidants affect the oxygen-atom transfer ability? A computational study. *Chem. Eur. J.* 2013, *19*, 4058–4068.

(93) Wojdyla, Z.; Borowski, T. On how the binding cavity of AsqJ dioxygenase controls the desaturation reaction regioselectivity: a QM/MM study. *J. Biol. Inorg. Chem.* 2018, *23*, 795–808.

(94) Prat, I.; Company, A.; Postils, V.; Ribas, X.; Que Jr, L.; Luis, J. M.; Costas, M. The mechanism of stereospecific C–H oxidation by Fe(Pytacn) complexes: Bioinspired non-heme iron catalysts containing cis-labile exchangeable sites. *Chem. Eur. J.* 2013, *19*, 6724–6738.

(95) Mukherjee, G.; Alili, A.; Barman, P.; Kumar, D.; Sastri, C. V.; de Visser, S. P. Interplay between steric and electronic effects: A joint spectroscopy and computational study of non-heme iron(IV)-oxo complexes. *Chem. Eur. J.* 2019, *25*, 5086–5098.

(96) Ye, S.; Geng, C-Y.; Shaik, S.; Neese, F. Electronic structure analysis of multistate reactivity in transition metal catalyzed reactions: the case of C−H bond activation by non-heme iron (IV)−oxo cores. *Phys. Chem. Chem. Phys.* 2013, *15*, 8017–8030.

(97) Cantú Reinhard, F. G.; Sainna, M. A.; Upadhyay, P.; Balan, G. A.; Kumar, D.; Fornarini, S.; Crestoni, M. E.; . de Visser, S. P. A systematic account on aromatic hydroxylation by a cytochrome P450 model Compound I: A low-pressure mass spectrometry and computational study. *Chem. Eur. J.* 2016, *22*, 18608–18619.

(98) Bernasconi, L.; Baerends, E. J. A frontier orbital study with ab initio molecular dynamics of the effect of solvation on chemical reactivity: solvent-induced orbital control in FeO-activated hydroxylation reactions. *J. Am. Chem. Soc.* 2013, *135*, 8857–8867.

(99) Hirao, H.; Li, F.; Que Jr., L.; Morokuma, K. Theoretical study of the mechanism of oxoiron (IV) formation from H$_2$O$_2$ and a nonheme iron (II) complex: O−O cleavage involving proton-coupled electron transfer. *Inorg. Chem.* 2011, *50*, 6637–6648.

(100) Tang, H.; Guan, J.; Zhang, L.; Liu, H.; Huang, X. The effect of the axial ligand on distinct reaction tunneling for methane hydroxylation by nonheme iron (iv)−oxo complexes. *Phys. Chem. Chem. Phys.* 2012, *14*, 12863–12874.

(101) Zhao, J.; Sun, X.; Huang, X.; Li, J. Reaction mechanisms of methanol oxidation by Fe^{IV}O biomimetic complex. *Int. J. Quantum Chem.* 2016, *116*, 692–701.

(102) Ansari, A.; Kaushik, A.; Rajaraman, G. Mechanistic insights on the ortho-hydroxylation of aromatic compounds by non-heme iron complex: A computational case study on the comparative oxidation ability of ferric-hydroperoxo and high-valent Fe^{IV}=O and Fe^{V}=O intermediates. *J. Am. Chem. Soc.* 2013, *135*, 4235–4249.

(103) Usharani, D.; Janardanan, D.; Li, C.; Shaik, S. A theory for bioinorganic chemical reactivity of oxometal complexes and analogous oxidants: The exchange and orbital-selection rules. *Acc. Chem. Res.* 2013, *46*, 471–482.

(104) Sahu, S.; Quesne, M. G.; Davies, C. G.; Dürr, M.; Ivanović-Burmazović, I.; Siegler, M. A.; Jameson, G. N. L.; de Visser, S. P.; Goldberg, D. P. Direct observation of a non-heme iron(IV)-oxo complex that mediates aromatic C-F hydroxylation. *J. Am. Chem. Soc.* 2014, *136*, 13542–13545.

(105) de Visser, S. P. Propene activation by the oxo-iron active species of taurine/α-ketoglutarate dioxygenase (TauD) enzyme. How does the catalysis compare to heme-enzymes? *J. Am. Chem. Soc.* 2006, *128*, 9813–9824.

(106) Decker, A.; Rohde, J.-U.; Klinker, E. J.; Wong, S. D.; Que Jr., L.; Solomon, E. I. Spectroscopic and quantum chemical studies on low-spin Fe^{IV}O complexes: Fe–O bonding and its contributions to reactivity. *J. Am. Chem. Soc.* 2007, *129*, 15983–15996.

(107) de Visser, S. P. Substitution of hydrogen by deuterium changes the regioselectivity of ethylbenzene hydroxylation by an oxo−iron−porphyrin catalyst. *Chem. Eur. J.* 2006, *12*, 8168–8177.

(108) Rétey, J. Enzymic reaction selectivity by negative catalysis or how do enzymes deal with highly reactive intermediates? *Angew. Chem. Int. Ed.* 1990, *29*, 355-361.

(109) Vögeli, B.; Erb, T. B. 'Negative' and 'positive catalysis': complementary principles that shape the catalytic landscape of enzymes. *Curr. Opin. Chem. Biol.* 2018, *47*, 94-100.

(110) Chua, C. S.; Biermann, D.; Goo, K. S.; Sim, T. S. Elucidation of active site residues of *Arabidopsis thaliana* flavonol synthase provides a molecular platform for engineering flavonols. *Phytochem.* 2008, *69*, 66-75.

(111) Welford, R. W. D.; Turnbull, J. J.; Claridge, T. D. W.; Prescott, A. G.; Schofield, C. J. Evidence for oxidation at C-3 of the flavonoid C-ring during anthocyanin biosynthesis. *Chem. Commun.* 2001, 1828-1829.

(112) Prescott, A. G.; Stamford, N. P. J.; Wheeler, G.; Firmin, J. L. In vitro properties of a recombinant flavonol synthase from *Arabidopsis thaliana*. *Phytochemistry* 2002, *60*, 589-593.

(113) Lukačin, R.; Wellmann, F.; Britsch, L.; Martens, S.; Matern, U. Flavonol synthase from *Citrus unshiu* is a bifunctional dioxygenase. *Phytohemistry* 2003, *62*, 287-292.

(114) Border, Z.-M.; Marais, C.; Bezuidenhoudt, B. C. B.; Jacobus A. Steenkamp, J. A. Studies Towards the stereoselective-hydroxylation of flavanones. Biosynthetic significance. *Aust. J. Chem.* 2008, *66*, 122-130.

(115) Han, X.-J.; Wu, Y.-F.; Gao, S.; Yu, H.-N.; Xu, R.-X.; Lou, H.-X.; Cheng, A.-X. Functional characterization of a *Plagiochasma appendiculatum* flavone synthase I showing flavanone 2-hydroxylase activity. *FEBS Lett.* 2014, *588*, 2307-2314.

(116) de Visser, S. P.; Tan, L. S. Is the bound substrate in nitric oxide synthase protonated or neutral and what is the active oxidant that performs substrate hydroxylation? *J. Am. Chem. Soc.* 2008, *130*, 12961-12974.

(117) Timmins, A.; Quesne, M. G.; Borowski, T.; de Visser, S. P. Group transfer to an aliphatic bond: A biomimetic study inspired by nonheme iron halogenases. *ACS Catal.* 2018, *8*, 8685–8698.

(118) Mayer, J. M. Proton-coupled electron transfer: A reaction chemist's view. *Annu. Rev. Phys. Chem.* 2004, *55*, 363-390.

(119)   Friedrich, L. E. The two hydrogen-oxygen bond-dissociation energies of hydroquinone. *J. Org. Chem.* 1983, *48*, 3851–3852.

(120)   Bordwell, F. G.; Cheng, J.-P. Substituent effects on the stabilities of phenoxyl radicals and the acidities of phenoxyl radical. *J. Am. Chem. Soc.* 1991, *113*, 1736–1743.

(121)   Mayer, J. M. Hydrogen atom abstraction by metal−oxo complexes: Understanding the analogy with organic radical reactions. *Acc. Chem. Res.* 1998, *31*, 441–450.

(122)   de Visser, S. P.; Kumar, D.; Cohen, S.; Shacham, R.; Shaik, S. A predictive pattern of computed barriers for C–H hydroxylation by Compound I of cytochrome P450. *J. Am. Chem. Soc.* 2004, *126*, 8362–8363.

(123)   Shaik, S. Kumar, D.; de Visser, S. P. A valence bond modeling of trends in hydrogen abstraction barriers and transition states of hydroxylation reactions catalyzed by cytochrome P450 enzymes. *J. Am. Chem. Soc.* 2008, *130*, 10128–10140.

(124)   de Visser, S. P. Trends in substrate hydroxylation reactions by heme and nonheme iron(IV)-oxo oxidants give correlations between intrinsic properties of the oxidant with barrier height. *J. Am. Chem. Soc.* 2010, *132*, 1087–1097.

(125)   Timmins, A.; Saint-André, M.; de Visser, S. P. Understanding how prolyl-4-hydroxylase structure steers a ferryl oxidant toward scission of a strong C–H bond. *J. Am. Chem. Soc.* 2017, *139*, 9855–9866.

Table Of Contents Graphic